

Seismic Tomography of the Southern California Plate Boundary Region from Noise-Based Rayleigh and Love Waves

DIMITRI ZIGONE,¹ YEHUDA BEN-ZION,¹ MICHEL CAMPILLO,² and PHILIPPE ROUX²

Abstract—We use cross-correlations of ambient seismic noise between pairs of 158 broadband and short-period sensors to investigate velocity structure over the top 5–10 km of the crust in the Southern California plate boundary region around the San Jacinto Fault Zone (SJFZ). From the 9-component correlation tensors associated with all station pairs we derive dispersion curves of Rayleigh and Love wave group velocities. The dispersion results are inverted first for Rayleigh and Love waves group velocity maps on a $1.5 \times 1.5 \text{ km}^2$ grid that includes portions of the SJFZ, the San Andreas Fault (SAF), and the Elsinore fault. We then invert these maps to 3D shear wave velocities in the top ~ 7 km of the crust. The distributions of the Rayleigh and Love group velocities exhibit 20 azimuthal anisotropy with fast directions parallel to the main faults and rotations in complex areas. The reconstructed 3D shear velocity model reveals complex shallow structures correlated with the main geological units, and strong velocity contrasts across various fault sections along with low-velocity damage zones and basins. The SJFZ is marked by a clear velocity contrast with higher V_s values on the NE block for the section SE of the San Jacinto basin and a reversed contrast across the section between the San Jacinto basin and the SAF. Velocity contrasts are also observed along the southern parts on the SAF and the Elsinore fault, with a faster southwest block in both cases. The region around the Salton Trough is associated with a significant low-velocity zone. Strong velocity reductions following flower-shape with depth are observed extensively around both the SJFZ and the SAF, and are especially prominent in areas of geometrical complexity. In particular, the area between the SJFZ and the SAF is associated with an extensive low-velocity zone correlated with diffuse seismicity at depth, and a similar pattern including correlation with deep diffuse seismicity is observed on a smaller scale in the trifurcation area of the SJFZ. These results augment local earthquake tomography images that have low resolution in the top few km of the crust, and provide important constraints for studies concerned with behavior of earthquake ruptures, generation of rock damage, and seismic shaking hazard in the region.

Key words: Noise-based imaging, Rayleigh and Love waves, San Jacinto fault zone region, seismic velocity contrasts, low-velocity zones, azimuthal anisotropy.

1. Introduction

Crustal fault zones have complex distributions of seismic properties that may include hierarchical damage zones, bimaterial interfaces, deformation structures, for example basins and ridges, and adjacent blocks with a variety of geological units and multi-scale heterogeneities. Imaging the fault zone velocity structure and the surrounding environment can provide important information for numerous topics ranging from the long-term evolution of the fault system to likely earthquake behavior and expected seismic shaking hazard (e.g. BEN-ZION 2008, and references therein). In this paper we present noise-based tomography of the shallow crust in the Southern California plate boundary region, focusing on the San Jacinto Fault Zone (SJFZ). The results complement recent double-difference tomography of earthquake arrival times in the area that show clearly along-strike and depth variations of fault damage zones, velocity contrasts, and other features of interest over a depth range of approximately 3–15 km (ALLAM and BEN-ZION 2012; ALLAM *et al.* 2014). The noise-based tomography of the present work allows us to obtain reliable results for the top few km, where the earthquake ray-coverage is sparse, and to image a somewhat broader region than that analyzed in the tomography studies cited above. Imaging the top few km of the crust is particularly important for understanding site effects that can significantly affect near-fault seismic ground motion (e.g. BOORE 2014; KURZON *et al.* 2014).

Electronic supplementary material The online version of this article (doi:10.1007/s00024-014-0872-1) contains supplementary material, which is available to authorized users.

¹ Department of Earth Sciences, University of Southern California, Los Angeles, CA 90089-0740, USA. E-mail: zigone@usc.edu

² Institut des Sciences de la Terre, Université Joseph Fourier, CNRS, IRD, BP 53, 38041 Grenoble, France.

Ambient noise tomography has developed substantially in recent years (see CAMPILLO *et al.* 2011, and references therein). Instead of using impulse sources, noise-based imaging involves extracting phase information between pairs of stations from correlations of a diffuse random wavefield. SHAPIRO and CAMPILLO (2004) and later work showed that the dispersion curves extracted from noise correlation functions are similar to those obtained from earthquakes. This allows the use of conventional surface wave tomography techniques to produce group or phase velocity maps of regions covered by a dense seismic network (e.g. SHAPIRO *et al.* 2005; SABRA *et al.* 2005a, b; LIN *et al.* 2007, 2008; MOSCHETTI *et al.* 2007; YANG *et al.* 2007; STEHLY *et al.* 2009; ROUX *et al.* 2011). The primary advantage of this method is the existence of ambient seismic noise in all places, albeit with strong spatio-temporal variations (e.g. STEHLY *et al.* 2006; KIMMAN and TRAMPERT 2010; LANDÈS *et al.* 2010; HILLERS and BEN-ZION 2011) that should be accounted for in the imaging analysis.

In a recent study HILLERS *et al.* (2013) investigated the feasibility of using ambient noise correlations to image the shallow structures of the SJFZ region. They found that the noise field in that area is sufficiently sensitive to existing structures and that consistent velocity measurements can be extracted from the cross-correlations of the ambient seismic noise. In the following sections we perform detailed analysis of noise cross-correlations from 158 stations in the plate-boundary region in southern CA. The noise cross-correlations are processed to retrieve Rayleigh and Love wave velocities, which are then used to obtain tomographic images of the region. In the next section we describe, briefly, the area under investigation and results from previous imaging studies. In Sect. 3 we outline the data and pre-processing used to compute the cross-correlations, and discuss potential effects of the directionality of noise sources on the cross-correlation functions. In Sect. 4 we describe the methods used to extract dispersion curves from the cross-correlations and azimuthal anisotropy of the group velocity results. In Sect. 5 we discuss the tomography formalism applied for inverting the dispersion results to shear wave velocities and present the

tomographic images obtained for the plate boundary region around the SJFZ. The results are discussed and summarized in Sect. 6.

2. The Study Area

The San Jacinto fault zone (Fig. 1) is one of several major right-lateral strike-slip structures over which the motion between the North American and Pacific plates is accommodated in southern California. It formed 1–2 million years ago, presumably in response to geometrical complexities on the San Andreas Fault (SAF), for example the San Geronio bend (e.g. MORTON and MATTI 1993; FIALKO *et al.* 2005; JANECKE *et al.* 2010), and is currently the most seismically active fault zone in southern California (HAUKSSON *et al.* 2012). The SJFZ effectively straightens the boundary between the North America and Pacific plates; its slip rate is currently similar to that of the southern SAF (e.g. FAY and HUMPHREYS 2005; LINDSEY and FIALKO 2013). A smaller part of the plate motion in the area is also accommodated by the Elsinore Fault located southwest of the SJFZ.

The structurally complex SJFZ consists of multiple segments (Fig. 1) with distinct surface expression and different seismic and geometrical properties (e.g. LEWIS *et al.* 2005; WECHSLER *et al.* 2009; SALISBURY *et al.* 2012). Over the past 1.5 Ma the fault has accommodated approximately 24 km of total displacement (SHARP 1967; ROCKWELL *et al.* 1990; KIRBY *et al.* 2007). The central portion of the SJFZ, often called the Anza section, is the most geometrically simple region with only a single active surface trace, the Clark Fault (CL). Paleoseismic trench sites at different locations along the Clark Fault indicate that it has a complicated rupture history featuring both large through-going events and segmented smaller ruptures (SALISBURY *et al.* 2012; MARILYANI *et al.* 2013; ROCKWELL *et al.* 2014). The Anza section has a clear across-fault velocity contrast over the seismogenic zone (ALLAM and BEN-ZION 2012) and, on the basis of tomographic images and direct small-scale geological mapping, asymmetry of rock damage in the shallow crust (DOR *et al.* 2006).

Southeast of Anza is the Trifurcation Area, where the Coyote Creek (CC) and Buck Ridge (BR)

Seismic Tomography of the Southern California Plate Boundary Region

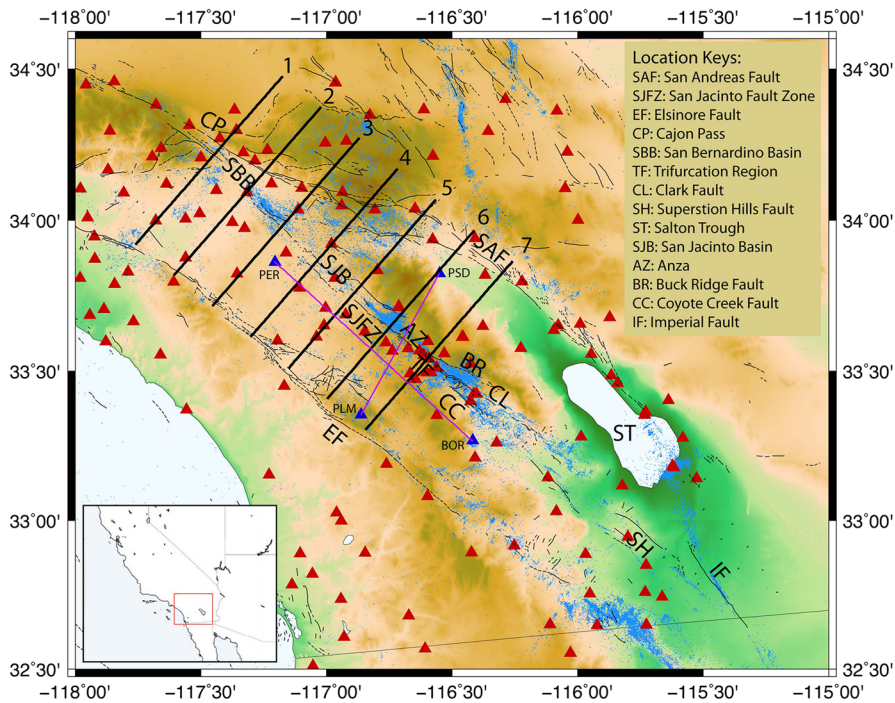


Figure 1

Map of the southern California plate boundary region with the 158 seismic stations used in this study (red triangles). The fine black lines indicate fault traces with the San Andreas Fault (SAF), the San Jacinto Fault Zone (SJFZ), and the Elsinore Fault (EF). The blue dots show the seismicity (HAUKSSON *et al.* 2012). The blue triangles are the example stations (paths in purple) discussed in Fig. 2. Cross-sections of velocity along profiles 1–7 (black lines) are shown in Figs. 14 and 15. The background colors indicate the topography, with green and brown being low and high elevations respectively. The inset indicates the location of the main map in California

segments branch off at low angles from the Clark fault. Although they vary in age and cumulative slip, all three segments are currently seismically active, as is evident from a cloud of distributed seismicity throughout the Trifurcation Area. The complicated geometry is also likely to be responsible for the highly heterogeneous focal mechanisms (BAILEY *et al.* 2010; HAUKSSON *et al.* 2012) in that region. Pronounced lithology contrasts in the surface geology are observed across all three fault strands (SHARP 1967; MORTON *et al.* 2012), with contacts between sedimentary and crystalline rocks in a variety of along-strike locations. The double-difference tomographic images show clear velocity contrasts across all three faults, and a low-velocity zone approximately 4 km-wide with a high V_p/V_s ratio in the trifurcation itself (ALLAM and BEN-ZION 2012; ALLAM *et al.* 2014). Detailed studies examining the geomorphology (WECHSLER *et al.* 2009) and seismic trapping structures (LEWIS *et al.* 2005; YANG and ZHU 2010) in the

area demonstrated the existence of asymmetric rock damage in the shallow crust, with more damage on the NE sides of each fault.

Northwest of Anza is the Hemet Stepover, a releasing step associated with the San Jacinto basin, where slip is transferred from the Claremont segment to the Casa Loma–Clark segment. Although the surface traces are distinct, paleoseismic work indicates that the two segments can rupture in a single through-going event (e.g. SALISBURY *et al.* 2012; ROCKWELL *et al.* 2006; MARILYANI *et al.* 2013). Compressional features at the Northwestern tip of the Casa Loma fault (BEN-ZION *et al.* 2012), in an area of otherwise extensional deformation, demonstrate the complexity of the system as a whole. The seismicity to the southeast of the Hemet Stepover is diffuse and associated with several oblique-slip anastomosing fault segments partly responsible for the uplift of the San Jacinto and Santa Rosa Mountains (ONDERDONK 1998). This complex region is associated with a zone

of low seismic velocities approximately 10 km wide, variations of the velocity contrast across the fault, and a low V_P/V_S ratio around the San Jacinto basin (ALLAM AND BEN-ZION 2012; ALLAM *et al.* 2014).

The SJFZ joins the SAF at its northern termination at Cajon Pass where both faults cut through the Transverse Ranges. The pass separates the San Bernardino Mountains to the east from the San Gabriel range to the west. The presence of the San Bernardino basin leads to a reversal of the velocity contrast across portions of the SJFZ in that section and a variety of other complexities (ALLAM and BEN-ZION 2012). Geologically mapped surface traces of the SJFZ and the SAF at the junction are separated by a few km, but along-fault variations of slip suggest that the fault systems are linked, with strain transfer on to the SJFZ probably contributing to the decrease in slip on the SAF from 24 ± 3.5 mm/year at Cajon Pass down to 5–10 mm/year at San Gorgonio Pass to the southeast (DAIR and COOKE 2009; SEEBER and ARMBRUSTER 1995; ZOBACK and HEALY 1992). The junction also marks a transition from a vertical SAF to the NW to a dip that has been inferred to be as shallow as $37 \pm 5^\circ$ to the SE (FUIS *et al.* 2012). Seismicity patterns in the region around Cajon Pass are complicated, with abrupt across-fault steps in maximum hypocentral depth (MAGISTRALE and SANDERS 1996; YULE and SIEH 2003).

3. Data, Noise Processing, and Cross-Correlations

3.1. Data and Noise Pre-Processing

We use continuous seismic data recorded during 2012, from January 1 to December 31, at 158 stations (Fig. 1) of the various seismic networks of southern California (the California Integrated Seismic network, the Anza network, the UC Santa Barbara Engineering Seismology network and the SJFZ Continental Dynamics project network). The combined network includes broadband (sampling rate 40 Hz) and short period (200 Hz) sensors distributed over the plate boundary region in southern California with inter-station distances ranging from ~ 1 km to ~ 300 km.

Imaging the subsurface structure using noise-based surface wave tomography requires pre-processing and multiple analysis steps to increase the quality of determination of phase arrivals and dispersion curves (e.g. SHAPIRO and CAMPILLO 2004; BENSEN *et al.* 2007; POLI *et al.* 2012; BOUÉ *et al.* 2013). In the following, we apply a modified version of the pre-processing procedure of POLI *et al.* (2012), which uses energy tests on short time windows to remove the effects of transient sources (earthquakes) and instrumental problems (gaps). We found by experimenting with the method version described below that it is an efficient tool for producing time series without obvious earthquake signals in our study area with high seismic activity, leading to cross-correlations with high signal-to-noise ratio (SNR) defined here as maximum amplitude divided by the standard deviation of the noise.

Signal pre-processing is done station by station in the following order:

1. the 24-h records are deconvolved from the instrument responses to ground velocity;
2. the data are high-pass filtered at 100 s and are clipped at 15 standard deviations to remove glitches resulting from the digitalization;
3. to remove additional instrumental problems and transient sources, for example earthquakes, the 24-h traces are then cut into 4-h sub-segments on which selection tests are performed; if the number of gaps exceeds 10 % of a sub-segment, the segment is removed; all segments with energy (integral over the segment of the waveform amplitude square) larger than twice the standard deviation of energy over the entire day are removed
4. the spectra of the remaining records are whitened by dividing the amplitude of the noise spectrum by its absolute value between 0.5 and 80 s without changing the phase;
5. to ensure that small earthquake signals are generally removed, we perform a second more standard clipping of the resulting waveforms at four standard deviations of the amplitudes;
6. the data are down-sampled to 4 Hz to reduce the size of the files;

7. Finally, we compute the cross-correlations between the corresponding segments at pairs of stations in the frequency domain as in [BENSEN *et al.* \(2007\)](#).

The correlation function for each day is the average of the segments remaining after the above pre-processing for that day. Because most of our stations record three components signals, we compute the nine inter-component (vertical (Z), North–South (N) and East–West (E)) correlation functions corresponding to the elastic Green’s tensor (ZZ, ZE, ZN, EZ, EE, EN, NZ, NE, NN). This correlation tensor is then rotated along the inter-stations azimuth to provide the correlation functions between the radial (R), transverse (T), and vertical (Z) components (RR, RT, RZ, TR, TT, TZ, ZR, ZT, ZZ) of the seismic wavefield propagating along the great circle connecting the two stations.

The main purpose of this pre-processing procedure ([POLI *et al.* 2012](#)) is to remove as many transient sources from the noise data as possible. Figures S1 and S2 illustrate the improvement in the surface wave reconstruction (e.g., signal-to-noise ratios, reasonable arrivals on positive and negative times, dispersion) compared with usual methods based on whitening and cutting the traces according to a pre-determined threshold (e.g. [BENSEN *et al.* 2007](#); [STEHLY *et al.* 2009](#), [HILLERS *et al.* 2013](#)). Figure S1a presents a day of data with an earthquake and Fig. S1b shows the corresponding waveform for which classical clipping (here at four standard deviations) was used to clean the time series. With such standard clipping, the earthquake signal is not fully removed from the data. This is better shown in Fig. S2a, which compares the cross-correlation for that particular “earthquake day” (red trace) and a reference day (blue trace) without a visible earthquake. The correlation function for the earthquake day is different from the one obtained with the cleaner noise wave field. In the former case, surface waves are masked by earthquake signals that produce a high-amplitude localized pulse that dominates the noise-scattered wave field. With the modified [POLI *et al.* \(2012\)](#) procedure used here, the last segment with the earthquake is removed (Fig. S1c). The correlation function computed after this treatment (red trace in Fig. S2b) is substantially improved, with clear arrivals in both positive and negative times as in the reference noise day (blue trace) compared with the results in Fig. S2a.

3.2. Surface Waves Reconstruction and Noise Directionality

Figure 2a and d show examples of ZZ daily correlation functions, presented as correlograms for different Julian days in 2012, between stations PLM–PSD (left) and stations PER–BOR (right). We choose these pairs of stations (the locations are given in Fig. 1) to illustrate two particular propagation directions: the paths between PLM–PSD and PER–BOR are, respectively, normal and parallel to the coast (which is the largest source of noise) and the SJFZ. Both correlograms show clear and stable arrivals at positive and negative times for the entire year (the asymmetry of the correlation functions observed for PLM–PSD and the reduced amplitudes for PER–BOR are discussed below). The temporal stability of the daily correlations indicates that most of the transient sources have been properly removed from the traces by the pre-processing, leading to stable arrivals in the correlation functions associated with the seismic wavefield propagating between the station pairs.

The daily correlations have 5–10 % amplitude variations without clear seasonal evolution, which may affect the quality of the cross-correlations by reducing the SNR for particular days, leading to less accurate traveltimes measurements. We remove these small-scale variations and increase the overall SNR by stacking the daily correlation functions for the whole year 2012 to obtain average ZZ correlations (top traces in Fig. 2b and e). Similar analyses give the average inter-component correlations between the vertical and radial (ZZ, ZR, RZ, RR) and transverse (TT) components (Fig. 2b and e). The arrival patterns observed for all correlation components in both the positive and negative times are dominated by surface waves traveling between the pairs of stations used. In both examples, the ZZ, ZR, RZ, and RR terms have Rayleigh waves with similar group time delays for all traces, and the expected phase shift because of the elliptical polarization of Rayleigh waves between the ZZ and RZ correlations. The TT correlations have Love waves.

Figure 2c and f present period–group velocity diagrams resulting from the combination of the ZZ, ZR, RZ, and RR components with a logarithmic stacking method described in Sect. 4.1. A clear

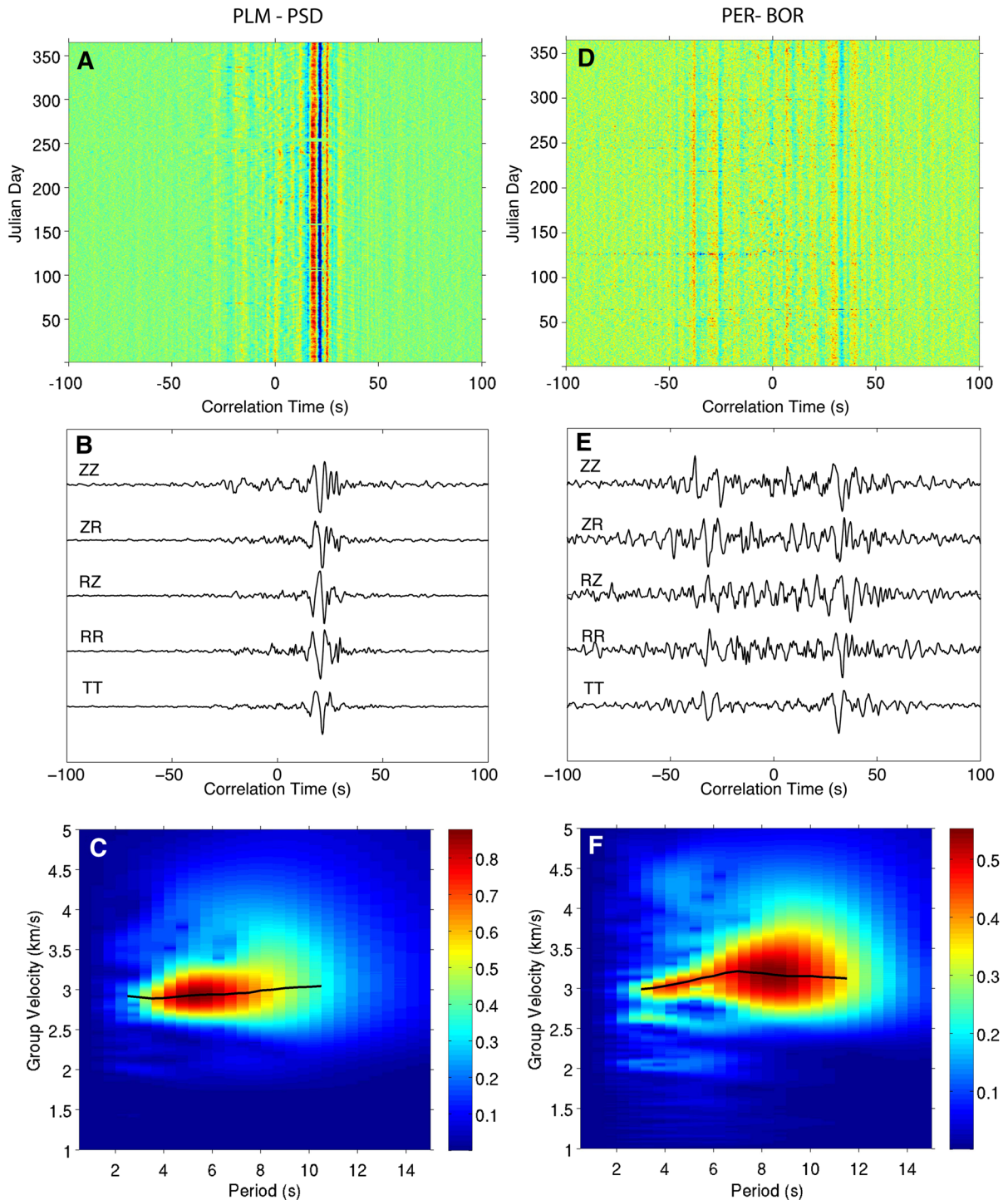


Figure 2

Examples of paths: PLM–PSD perpendicular to the coast and the SJFZ (*left*) and PER–BOR along these structures (*right*). The locations of the stations and the discussed paths are indicated in Fig. 1. Daily ZZ correlations are plotted as correlograms in (a) and (d). (b, e) Stacked cross-correlation for the entire year 2012 between PLM and PSD (b) and PER and BOR (e). The components are indicated in the figure. Rayleigh waves are observed on the ZZ, ZR, RZ, and RR components and Loves waves are obtained on the TT component. (c, f) Period–group velocity diagrams resulting from the combination of the ZZ, ZR, RZ, and RR components with a logarithmic stacking method described in Sect. 4.1.

The *black lines* indicate the measured Rayleigh waves dispersion curves and the range on which they are used in the inversion

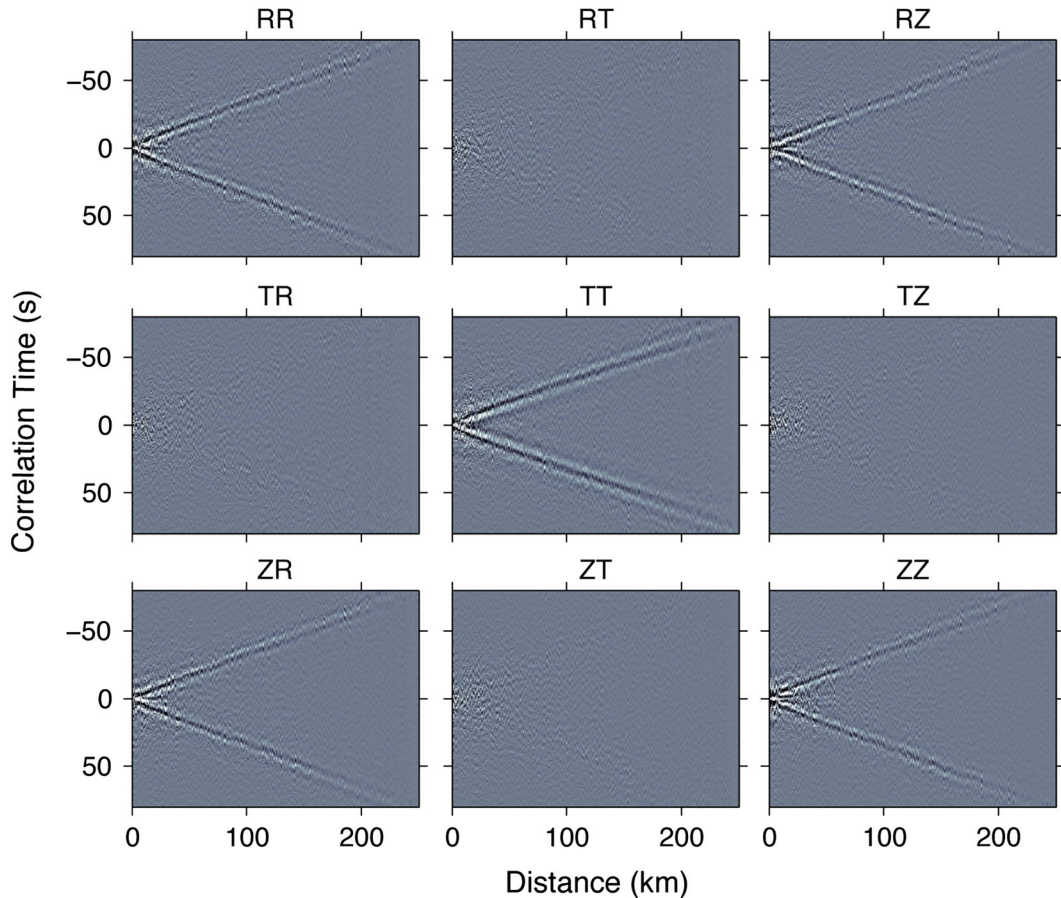


Figure 3

Correlation time in seconds as a function of inter-stations distance for the nine components of the correlation tensor (the components are indicated *above the panels*). The correlations are stacked for each 0.5 km distance bin. Clear Rayleigh waves are reconstructed on the RR, RZ, ZR, and ZZ components. Love waves are reconstructed on the TT component. Note the overall good symmetry of the correlations functions. *White and black* indicate positive and negative amplitudes, respectively, with the same scale in all panels

dispersive pattern corresponding to the fundamental Rayleigh wave mode is observed in both cases for periods between 3 and 12 s. The dispersion curves extracted from these period–group velocity diagrams (black lines in Fig. 2c and f) show different dispersion characteristics between the two paths (e.g., higher Rayleigh wave group velocities for PER–BOR compared with PLM–PSD, and more stable Rayleigh dispersion for PLM–PSD with a slightly increasing group velocity for increasing period), which reflect the different media sampled by the reconstructed Rayleigh waves traveling between PLM–PSD and PER–BOR.

Clear differences in term of amplitudes and symmetry are observed for the two propagation directions plotted in Fig. 2. The correlations for

coast-normal directions (left panels) reveal an asymmetric surface wave amplitude pattern whereas more symmetric correlation functions with reduced amplitudes are observed for the coast-parallel directions (right panels). This is explained by the dominance of near-coastal excitation of the noise field in southern California and a scattering mean free path that is too large to completely randomize the ambient noise (HILLERS *et al.* 2013). As a result, the amplitudes of the reconstructed surface waves are significantly higher for the west–east-propagation direction corresponding to the noise directionality between PLM and PMD. The lack of strong noise sources for coast-parallel directions explains the symmetry and overall amplitude reduction of the reconstructed surfaces

waves between PER and BOR. The non-isotropic distribution of noise sources may bias the measured travel times on correlation functions (e.g. WEAVER *et al.* 2009; FROMENT *et al.* 2010). HILLERS *et al.* (2013) studied the potential errors in arrival-time measurements of Rayleigh waves in the SJFZ region due to the directional noise and found the effect to be small. We note that the strong directional distribution of noise sources will mainly affect the coast-normal paths (Fig. 2). The distribution of 158 stations used in this work (Fig. 1) leads to a large number of paths in all directions, that helps obtaining reliable results for surface wave propagation in the region.

Figure 3 illustrates the propagation of the surface waves through the entire network, by showing the nine components of the correlation tensor as a function of inter-station distances. The correlations are stacked in 0.5 km distance bins for a better visualization. As for the two specific station pairs used for the examples in Fig. 2, prominent Rayleigh waves are reconstructed on the RR, ZZ, RZ, and ZR components and Love waves are reconstructed on the TT correlation term. Note the slightly faster Love waves. The remaining transverse components (RT, TR, TZ, ZT) show only weak diffuse phases, as expected theoretically, lending support to the quality of the rotations along the inter-station azimuth (discussed in Sect. 3.1). In the following sections we perform travel times measurements on the various components and use the data to obtain tomographic images for the region.

4. Surface Wave Tomography

In this section, we use Rayleigh and Love waves constructed from the ambient noise cross-correlations to image the shallow crust in the southern California plate-boundary region. We derive dispersion curves for all station pairs and then invert the dispersion curves first to group velocities and then to shear wave velocity maps for the region.

4.1. Dispersion Measurements and Paths Selection

Dispersion measurements are obtained for periods of 1–25 s from the reconstructed surface waves by using the frequency–time analysis (FTA) of LEVSHIN

et al. (1989). Dispersion analysis can be conducted on both the causal and anti-causal parts of the correlations. For Rayleigh waves, we take advantage of the four components of the correlation tensor (RR, ZZ, RZ, ZR) that contain Rayleigh waves. We first compute the FTA for each signal i , independently, to obtain a normalized period–group velocity diagram $N_i(T, u)$, where T is the period and u the group velocity. The results are then combined with a logarithmic stacking in the period–group velocity domain as in CAMPILLO *et al.* (1996).

$$A_s(T, u) = \prod_i N_i(T, u), \quad (1)$$

where $A_s(T, u)$ is the combined period–group velocity diagram on which the dispersions are calculated. The width of the mean envelope for a given period is proportional to the inverse of the number i of stacked FTA (8 in our case), and its amplitude depends on the standard deviation of the group velocities. The dispersion measurements are evaluated on the $[A_s(T, u)]^{(1/i)}$ diagram, which provides amplitude values between 0 and 1, independently of the number i of stacked FTA. We use only the period–group velocity region on the $[A_s(T, u)]^{(1/i)}$ diagram for each pair of stations that have maximum amplitude above 0.3. The same method is used to extract Love wave dispersion curves, using in that case only the two possible measurements (on the causal and anti-causal TT correlation). Given the different amounts of measurements, we expect generally more reliable results for Rayleigh waves than for Love waves.

This technique is used for data with sufficiently high SNR on both the causal and anti-causal parts of the correlation functions (Fig. 3), including paths with strongly asymmetric noise sources (e.g., the left panels of Fig. 2). Moreover, the logarithmic stacking method takes advantage of different frequency contents in the opposite propagation directions for some pairs of stations. Because of the dominant near-coastal excitations, the incident noise direction coming from the Pacific includes higher frequencies compared with the opposite direction (HILLERS *et al.* 2013). As illustrated in Fig. 2c and f, using combinations of the ZZ, ZR, RZ, and RR measurements on the positive and negative times, we obtain clear Rayleigh wave dispersion curves both for coast-normal and coast-parallel paths. If the measurements

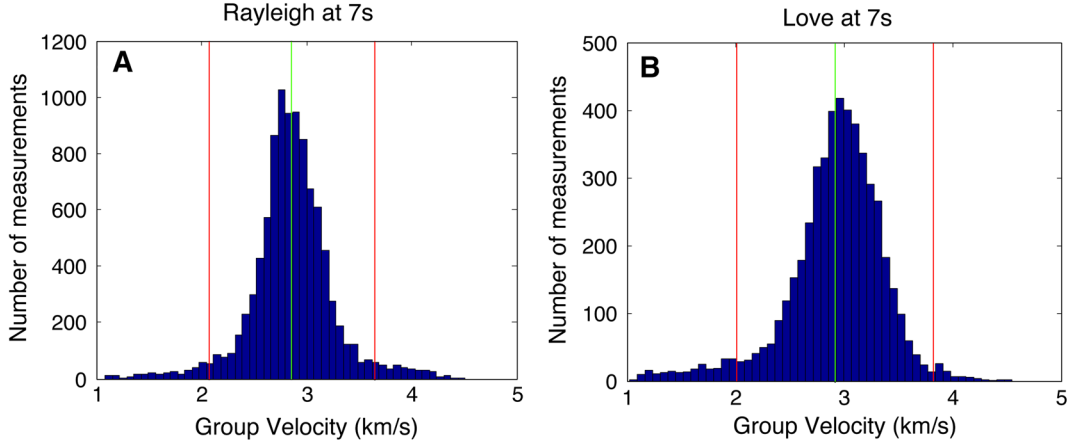


Figure 4

Histograms of dispersion measurements at 7 s for Rayleigh (a) and Love waves (b) for all pairs of stations. The *green lines* indicate the mean values and the *red lines* 2 standard deviations. Only measurements within these 2 standard deviations are used for the inversions

Table 1

Number of paths selected for each period

Period (s)	3	4	5	6	7	8	9	10	11	12
Love	2,410	3,068	3,176	3,122	3,014	2,858	2,577	2,322	1,896	1,457
Rayleigh	2,881	4,315	4,542	4,442	4,182	3,678	2,781	2,045	1,379	810

obtained from the opposite incident noise directions are not sufficiently similar, the resulting stacked period–group velocity diagram will not reach the threshold (here 0.3) to be considered in the tomography.

Figure 4 shows histograms of the measured group velocity for Rayleigh (Fig. 4a) and Love (Fig. 4b) waves at a period of 7 s for all pairs of stations. For Rayleigh waves, the measured velocity has a mean value of 2.86 km/s with a relatively symmetric spread associated with standard deviation of 0.39 km/s. For Love waves, the average velocity is 2.92 km/s with a more asymmetric spread and standard deviation of 0.45 km/s. The relatively large standard deviations are expected in the Southern California study region with strong lateral variations of velocities (ALLAM and BEN-ZION 2012). The more disordered results for Love waves compared with Rayleigh waves are expected from the smaller number of measurements. To increase the quality of the inversions, we require the measurements to satisfy three different criteria:

- First, we remove all correlation functions with a SNR < 7 to ensure that the travel times are well estimated.
- Second, for each measured period we exclude all paths with a length smaller than one wavelength. Because of the size of the area under investigation, we have a small number of paths for periods above 12 s (Table 1). Given this and our interest in the shallow crust, we focus on periods below 12 s.
- Finally, we keep only the velocity measurements in a range of two standard deviations from the mean (red vertical lines in Fig. 4a and b). This reduces the variability in the measurements and avoids unrealistic values for the inversion.

Table 1 summarizes the number of measurements selected for each period used in the inversions.

4.2. Azimuthal Anisotropy

Before inverting the data for isotropic velocity models, we analyze potential azimuthal anisotropy in the high-quality velocity measurements satisfying the

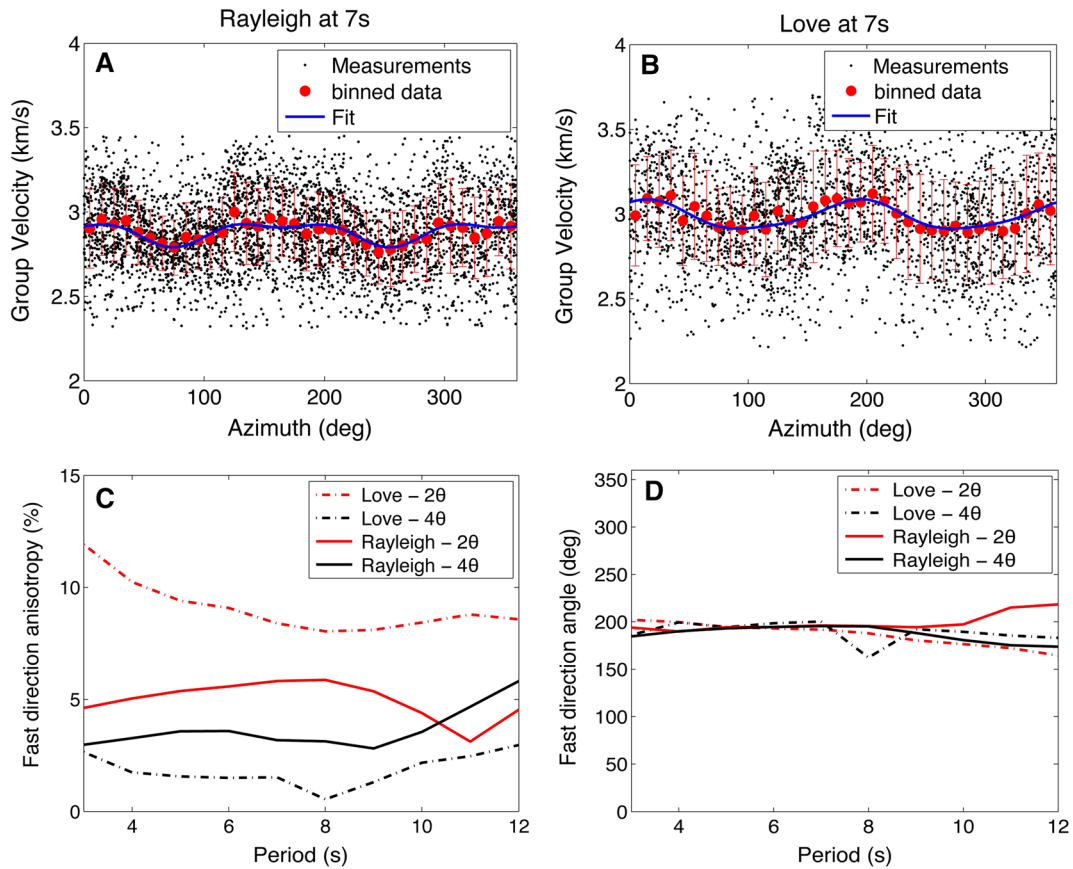


Figure 5

Azimuthal distributions of selected dispersions at 7 s (see Fig. 4) for Rayleigh (a) and Love (b) waves, respectively. The *small black dots* are the group velocity measurements. The *large red dots* are the group velocity averaged over 10° bins with *error bars* indicating standard deviations. The *thick blue curves* are the best fits for the 2θ and 4θ azimuthal variations obtained by Eq. (2). **c, d** Values of the fitted parameters as a function of period. **c** Values of A and B of Eq. (2) for Love (*dashed*) and Rayleigh (*continuous*) waves. **d** Best-fitting angles for Love (*dashed*) and Rayleigh (*continuous*) waves

criteria discussed above. This can augment the isotropic velocity models by providing information about the orientation of velocity variations in the southern California plate boundary area. Numerous studies have demonstrated the existence of seismic anisotropy in the shallow crust around fault zones from shear wave splitting in earthquake waveforms (e.g. ASTER *et al.* 1990; PENG and BEN-ZION 2004; LIU *et al.* 2005; BONESS and ZOBACK 2006; YANG *et al.* 2011). As the noise correlations are dominated by the fundamental mode of surface waves, we can use the selected group velocity measurements obtained from the cross-correlations to infer azimuthal anisotropy in the SJFZ region (e.g. LIN *et al.* 2009, 2011; FRY *et al.* 2010; MORDRET *et al.* 2013). Dispersive surface waves, which are sensitive to deeper structures for

increasing periods, may be used to retrieve the 3D distribution of azimuthal anisotropy.

Figure 5a and b display the azimuthal distribution of the group velocity measurements (Fig. 4) at 7 s for Rayleigh and Love waves (small black dots). The large red dots with error bars are group velocities averaged over 10° bins. The results reveal azimuthal dependence of values, with azimuths at approximately 10° and 200° showing significantly higher velocities for both Rayleigh and Love waves.

To study the azimuthal distribution, we use a parameterization similar to that of SMITH and DAHLEN (1973). For a slightly anisotropic medium, the group velocities can be approximated in the form of an even-order harmonic function with 180° (2θ anisotropy) and 90° (4θ anisotropy) periodicity:

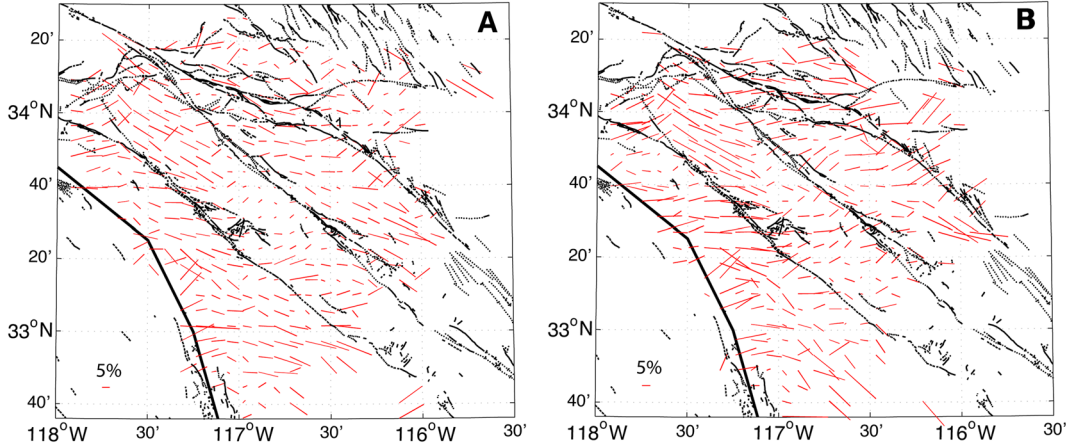


Figure 6

Azimuthal 2θ anisotropy maps with fast directions and amplitudes for 7 s Rayleigh (a) and Love (b) waves

$$U(\theta) = u_0 + A \cdot \cos(2(\theta - \varphi_2)) + B \cdot \cos(4(\theta - \varphi_4)), \quad (2)$$

where u_0 is the average group velocity, θ is the azimuth, A and B are peak-to-peak relative amplitudes of the 2θ and 4θ terms, and φ_2 and φ_4 define the orientation of the fast axes for the 2θ and 4θ terms. The blue lines in Fig. 5a and b show the optimum fit. The results indicate 2θ azimuthal anisotropy of 6–10 % for incident propagation directions oriented around 200° (Fig. 5c and d). The 4θ component is only a few percent and has maximum speed oriented in the same direction. We note that group velocities extracted from Love waves have higher (by approx. 4–5 %) 2θ anisotropy, which may reflect less reliable velocities based on only two independent measurements. The amplitudes and orientations found for both the average 2θ and 4θ terms are in general agreement with previous studies (e.g. LIN *et al.* 2011; RITZWOLLER *et al.* 2011). The origin of this average azimuthal anisotropy is not fully clear. One possible explanation is a bias due to the strongly asymmetric noise sources concentrated at the Pacific (e.g. HILLERS *et al.* (2013) and Sect. 3.2), which corresponds to the fast direction angle around 200° (Fig. 5d). A good test of this potential bias is to invert for the spatial distribution of the azimuthal anisotropy. If the strong directionality of noise sources biases the measurements we expect to find a coast-perpendicular fast direction for the entire map. In contrast, if the fast directions are affected by prominent structures (e.g. fault zones,

basins) this will suggest a physical origin related to the crustal properties.

To reduce the uncertainties, we combine all measurements within $8 \text{ km} \times 8 \text{ km}$ cells (LIN *et al.* 2009; MORDRET *et al.* 2013). The results in each cell are averaged on 20° azimuth bins and fitted by Eq. (2). We define the misfit of the inversion for a single cell as the standard deviation between the measured and predicted group velocities (MORDRET *et al.* 2013) and use for interpretation only the cells with a misfit smaller than 0.15 km/s. The resulting maps for the Rayleigh and Love waves are presented in Fig. 6. As found in previous studies (e.g. LIN *et al.* 2011; RITZWOLLER *et al.* 2011), we observe clear spatial variations with overall correlation between the 2θ fast direction orientation and major geological structures. LIN *et al.* (2011) used both noise correlations and earthquake data and found the same pattern of azimuthal anisotropy with fast directions that follow the main geological boundaries in southern California. The results in Fig. 6 provide additional details to the large scale analysis of LIN *et al.* (2011). The fast directions are usually aligned with the system of strike-slip faults that form the southern California plate boundary region, with some deviations related to structural complexities. Rotations of fast directions are observed for the region where the SJFZ and SAF merge and for other places with major fault branches. Around the Anza section of the SJFZ with relatively simple geometry, the degree of azimuthal anisotropy

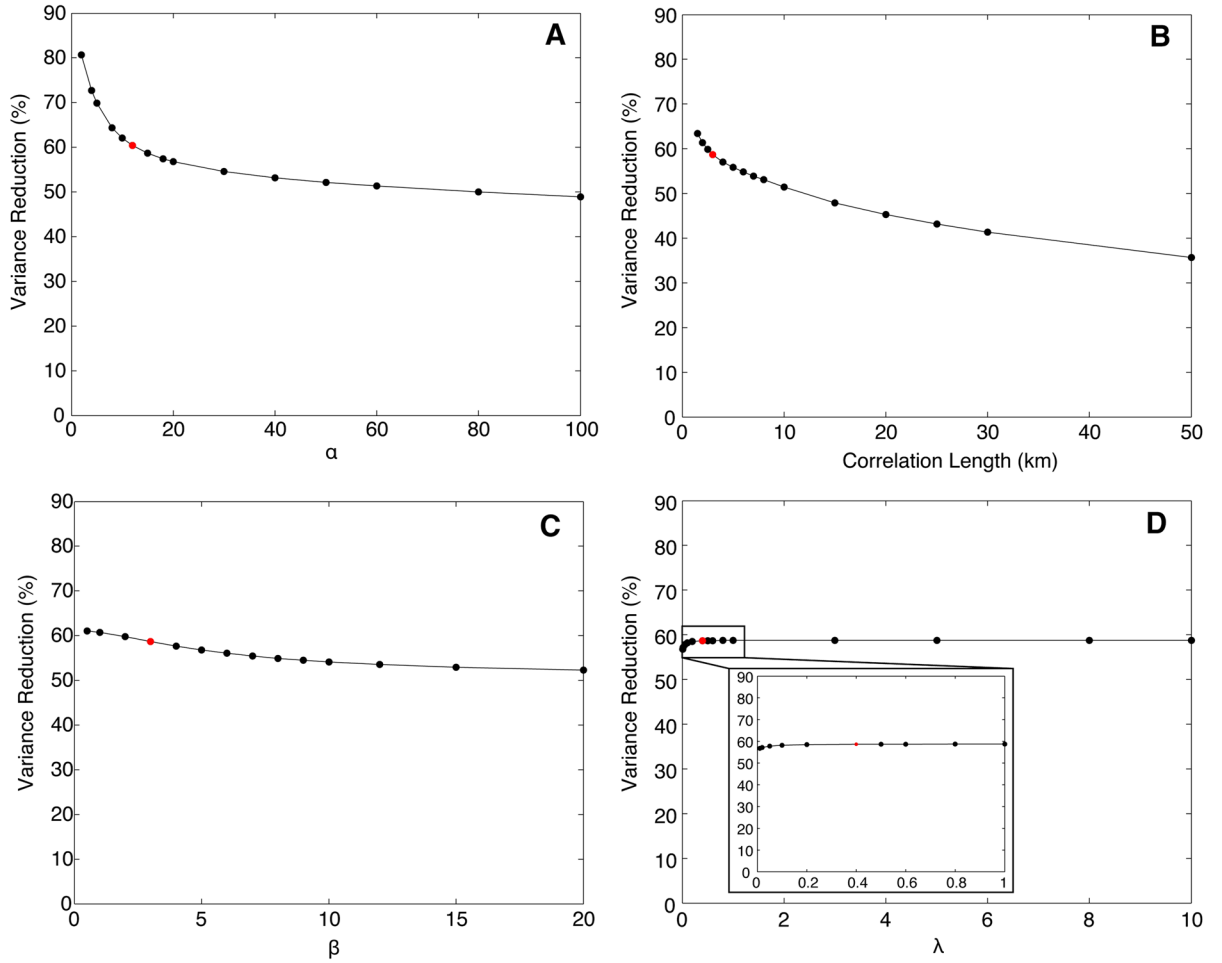


Figure 7

Variance reduction as a function of the four different parameters used in the inversion (L-curve analysis) for Rayleigh waves with a period of 7 s: **a** damping factor α , **b** correlation length σ , **c** β , and **d** λ . The chosen parameters are indicated by red dots. The inset in **d** provides a zoom in for λ values between 0 and 1

is much smaller than in structurally complex regions. The coast-perpendicular fast directions may be associated with rotations in areas with multiple complex structures, or reflect, in some places, artifacts related to the directionality of the noise sources.

4.3. Inversion of Dispersion Measurements for Group Velocities

The dispersion measurements are inverted to obtain isotropic group velocity maps following the BARMIN *et al.* (2001) method. The standard forward problem is written in tensor notation as:

$$d = Gm, \quad (3)$$

where $d = t^{\text{means}} - t^0$ is the data vector consisting of the differences between the measured group travel times and those computed with the initial model for each path. The matrix G represents the surface wave traveltimes for each path in each cell of the initial model. The inversion target is the group velocity map $m = (u - u_0)/u_0$, where u is the velocity obtained after inversion and u_0 the initial group velocity. For each period, the initial model over the entire region is the average value of all the measurements for that period.

The BARMIN *et al.* (2001) inversion is based on minimization of a penalty function having a linear combination of data misfits, magnitude of perturbation, and model smoothness:

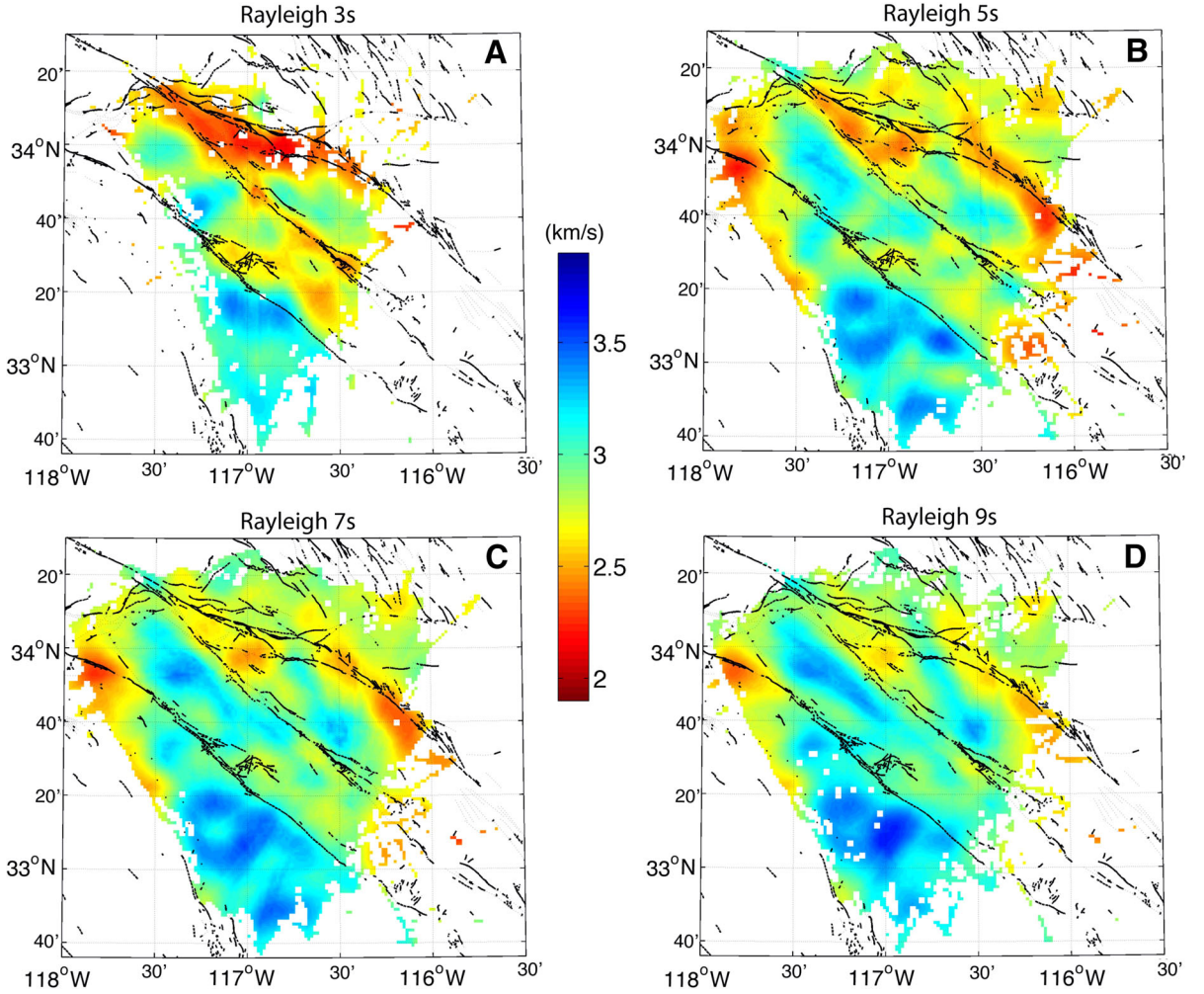


Figure 8

Rayleigh group velocity maps at 3 s (a), 5 s (b), 7 s (c), and 9 s (d). The colorbar shows the Rayleigh waves group velocities in km/s

$$(G(m) - d)^T (G(m) - d) + \alpha^2 \|F(m)\|^2 + \beta^2 \|H(m)\|^2, \quad (4)$$

where F is a Gaussian spatial smoothing function over the surface covered by the grid with correlation length σ written as:

$$F(m) = m(r) - \int_s \exp\left(-\frac{|r - r'|^2}{2\sigma^2}\right) \cdot m(r') dr', \quad (5)$$

and the last term H is defined as:

$$H(m) = \exp(-\lambda\rho) m, \quad (6)$$

where ρ is the path density (discussed further and illustrated in Sect. 4.4 below) and λ a weight

parameter that produces gradual fading of the inverted model into the initial model in areas where the path density is low.

Four parameters are used to regularize the solution: β and λ control the magnitude of the model perturbations and α and σ control the spatial smoothing. These parameters are chosen through a standard L-curve analysis by plotting the variance reduction as a function of the different parameters. The preferred values are usually chosen to be near the maximum curvature of the L-curves (e.g. HANSEN and O'LEARY 1993; STEHLY *et al.* 2009). This is illustrated in Fig. 7 for Rayleigh waves at a period of 7 s. The coefficients α and σ that control the smoothness

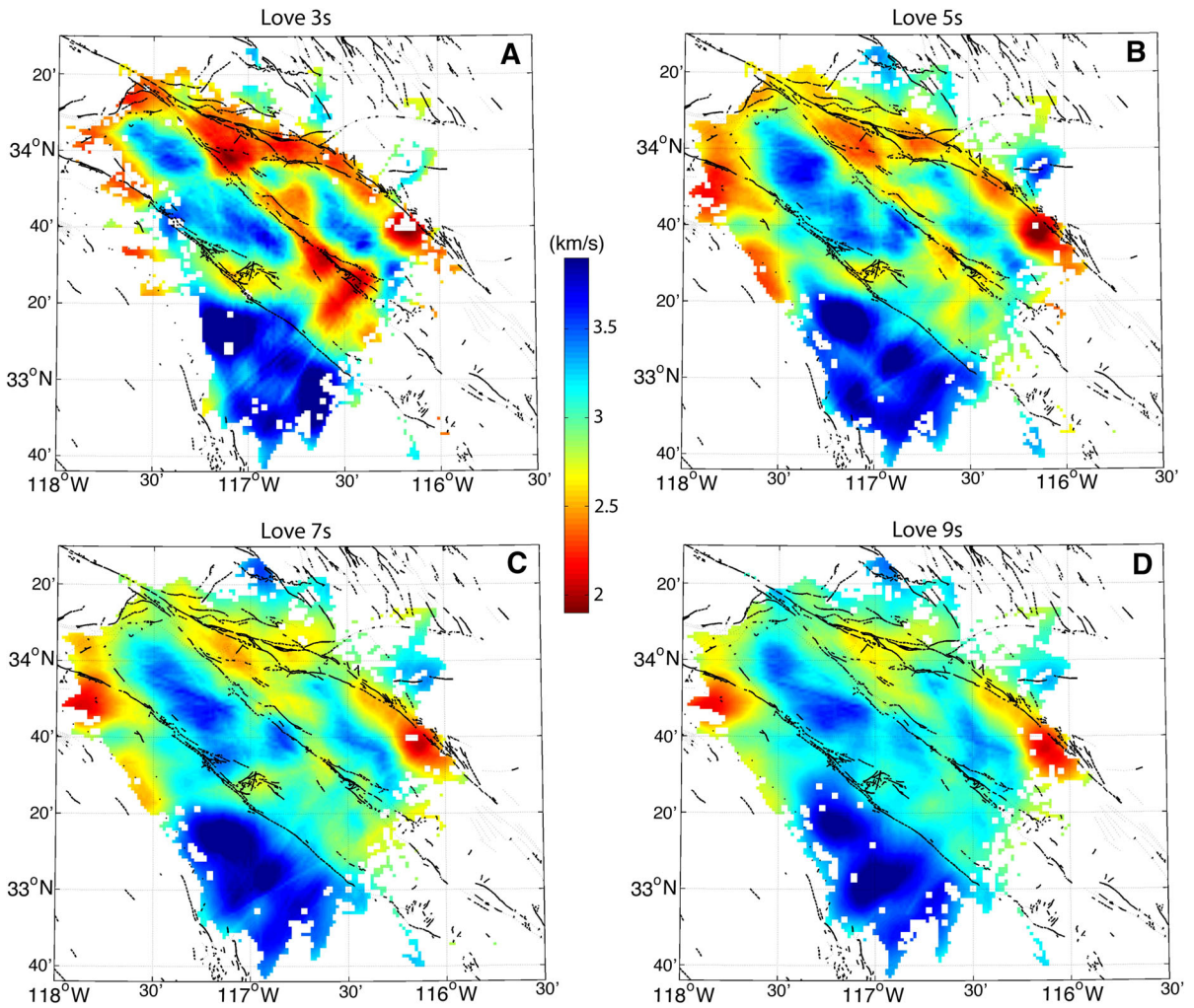


Figure 9

Love group velocity maps at 3 s (a), 5 s (b), 7 s (c), and 9 s (d). The colorbar shows the Love waves group velocities in km/s

strongly affect the variance reduction and the final inversion results. The damping factor α has period-dependant values determined by L-curve analysis (see the example at 7 s in Fig. 7a) and is 12 for periods from 3 to 11 s and 15 for a period of 12 s. This increase of α for 12 s is related to the lower quality of the data (i.e. number of paths), which requires slightly stronger smoothing to avoid the appearance of speckles in the maps. The correlation length σ is set at 3 km for all the frequencies, using again an L-curve criterion (Fig. 7b). Note that α and σ are not chosen to minimize the misfit (i.e. maximize the variance reduction), because for minimizing values the model results are contaminated by small-scale patterns associated with the path distribution. β

and λ have little effect on the inversions, because they affect only cells with low path coverage, and are fixed (Fig. 7c, d) at $\beta = 3$ and $\lambda = 0.4$. For inversions of Love waves, the parameters remain the same, except for α which is set to be 18 for all periods.

Figure 8 gives inverted group velocity maps at 3, 5, 7, and 9 s for Rayleigh waves and Fig. 9 provides corresponding maps for Love waves. The results show overall increasing velocities with periods associated with dispersion of the Rayleigh and Love waves. In addition, the images reflect a diversity of structural features including clear velocity contrasts across the main faults with low-velocity damage zones and basins. The low-velocity damage zones are especially pronounced at low

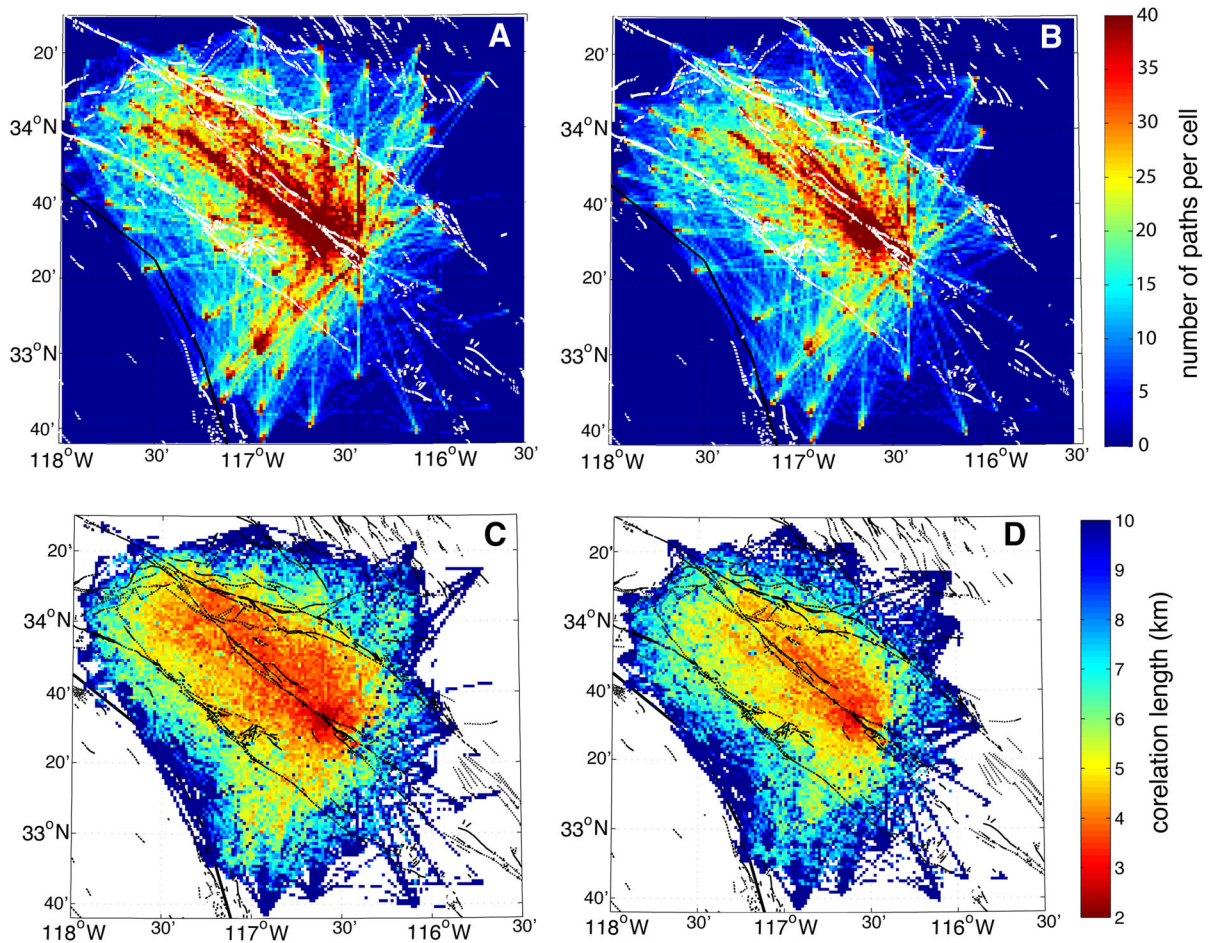


Figure 10

Number of paths per cell at 7 s for Rayleigh (a) and Love waves (b). Path coverage is high for all regions between the Elsinore Fault and the San Andreas Fault. c, d Value of the resolution length at 7 s for Rayleigh (c) and Love (d) waves. The resolution is good (small correlation length) for most of the region of interest with a mean correlation length of approximately 3–4 km. The resolution is lower for Love waves because of the smaller number of paths (4,182 paths for Rayleigh waves versus 3,014 paths for Love waves at 7 s; Table 1)

periods of Love waves in areas of structural complexity (e.g. the trifurcation area and region between the SAF and SJFZ); the low-velocity zone around the Salton trough persists for up to 9 s. The NE block of the SJFZ has higher group velocities than the SW block at periods up to 5 s, other than in the region between the SJFZ and SAF to the NW of the San Jacinto basin (Fig. 1) where the SW block has higher velocities. For periods longer than 5 s, the velocity contrast along the central SJFZ is small, whereas the SW block has higher group velocities to the NW of the San Jacinto basin. The group velocity maps also show a clear contrast across the southern SAF near the Salton

trough with a slower SW block, and across portion of the Elsinore fault with faster SW block up to periods of 7 s.

4.4. Inversion Resolution

The resolution of the inversion with the BARMIN *et al.* (2001) method is described by a resolution matrix that depends mostly on the network geometry and distribution of high-quality measurements that satisfy the criteria discussed in Sect. 3. The rows of the resolution matrix give the resolution of the final model at each cell by quantifying the dependency of the obtained group velocity at that location on the

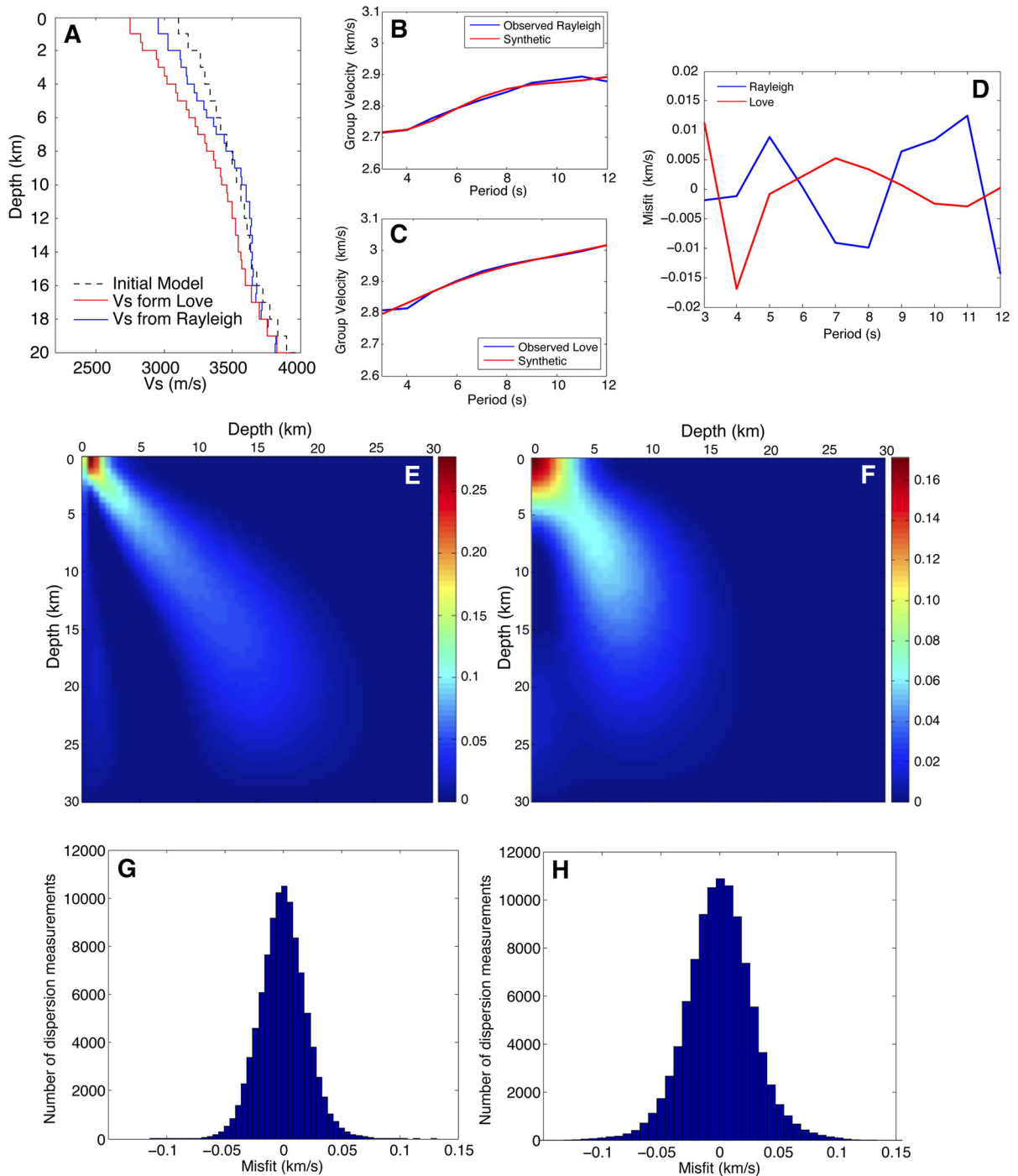


Figure 11

a Average shear wave velocity model of the area obtained from Rayleigh (*blue curve*) and Love (*red curve*) waves group velocity maps. The *dashed black line* shows the average ALLAM and BEN-ZION (2012) model used here as the initial model for the inversions. **b, c** Average dispersion curves (*blue line*) and theoretical curves associated with the models of (**a**) for Rayleigh (**b**) and Love (**c**) waves. **d** Misfit as a function of period between the two curves of (**b**) (*blue trace*) and (**c**) (*red trace*). **e, f** Resolution matrix of the average dispersion curves inversions for Rayleigh (**e**) and Love (**f**) waves. **g, h** Histograms of misfits for the local shear wave inversions using Rayleigh (**g**) and Love (**h**) waves dispersion curves. The *histograms* show the misfit between observed and synthetic dispersion curves for each cell when all the periods are considered

measurements at all other locations. The quality of the obtained maps can be assessed by using:

- the path density in each cell, and
- the resolution length at each node, defined as the distance for which the value in the resolution matrix decreased by a factor of 2.

Figure 10a and b show the path density in each cell of $1.5 \times 1.5 \text{ km}^2$ for the Rayleigh and Love waves obtained at 7 s. The path coverage in the region of interest from the Elsinore fault to the SAF is good, with more than 20 paths per cell. Close to the SJFZ, the path coverage increases to a minimum of 40 paths per cell with a maximum value of 164 paths. The only poorly resolved region is SE of the trifurcation area where the number of paths decreases rapidly because of the lack of stations in that region. Figure 10c and d present the correlation length in each model cell. There is good (relatively small) correlation lengths in the range 2–4 km in most of the region around the SJFZ, up to the SAF to the NE and the Elsinore fault to the SW. The resolution in the Salton trough is reduced with correlation lengths above 7 km, and is poor to the SE of the trifurcation area because of lack of data. We also note that the path coverage is lower and the correlation length is higher for Love waves, because results are for fewer cells than for the Rayleigh waves (Figs. 8, 9), which is related to the smaller number of measurements used to reconstruct the Love waves.

5. Inversions for 3D Shear-Wave Velocities

5.1. Inversion Method and Resolution

The group velocity maps obtained for each period are inverted for shear wave velocities using the linearized inversion scheme of HERMANN and AMMON (2002). Considering the period interval from 3 to 12 s for which we have reliable group velocity maps, we focus the inversion on the top ~ 7 km of the crust. This is an important depth range because the velocities structure in the top few km of the crust are typically not well constrained by earthquake tomography (e.g. ALLAM and BEN-ZION 2012). We first invert for an average depth-dependent V_s model and then use the local dispersion curves extracted

from the group velocity maps to obtain depth-dependent V_s profiles for each cell of the grid. By combining all local 1D profiles we obtain a detailed 3D shear wave velocity structure in the study region.

The quality of the inverted models with the linear approach of HERMANN and AMMON (2002) depends on the accuracy of the initial model. To have an good initial model we use the results from the double-difference earthquake tomography of ALLAM and BEN-ZION (2012), which provide detailed images of crustal velocities over the depth range ~ 3 to 15 km. We begin with a starting model that consists of laterally-average velocities from ALLAM and BEN-ZION (2012) in 60 layers with thickness values that vary from 500 m for the first 40 layers to 1 km for the others (Fig. 11a). With the limited depth resolution of the fundamental mode of the Rayleigh and Love waves for the periods considered, we impose smooth velocity variations with depth in the top 30 layers. The velocity is allowed to take a large range of values as long as the depth variation is smooth. The obtained results are well-defined solutions given the model parameterization, as discussed below.

Using the above initial model, we invert the average group velocity dispersion curves (Fig. 11b and c) to obtain related average crustal V_s models for the region (Fig. 11a). We compute the average dispersion curves by averaging the group velocity maps at each period in cells with path density above 5. Figure 11b and c show the average group velocity curves, with theoretical dispersion curves associated with the inverted Rayleigh and Love-based models of Fig. 11a. As shown in Fig. 11d, the results are well fitted, with a misfit of less than 0.015 km/s for both Rayleigh and Love waves. The depth resolution of the inversions in the 3–12 s periods range is relatively high over the shallow crust for both Rayleigh and Love waves. The resolution matrices presented in Fig. 11e and f indicate good resolution up to 7–10 km for Rayleigh waves and up to 5–7 km for Love waves. The V_s model based on the Love waves shows lower velocities by approximately 6 % in the shallow structures (Fig. 11a). This may stem from a combination of less reliable Love wave group velocities measurements and/or the existence of anisotropy. The path coverage, which is limited for Love waves on the model edges where low-velocity

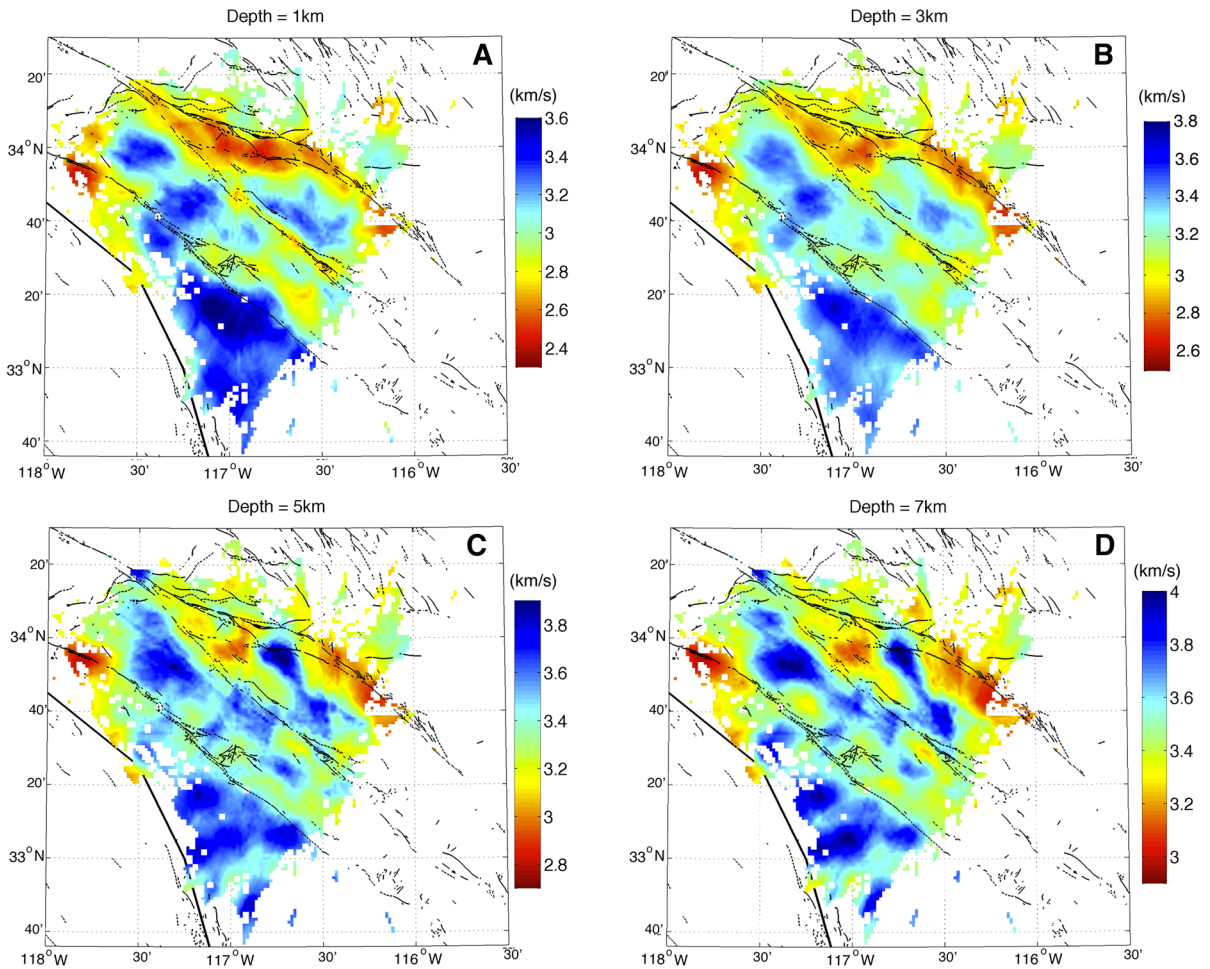


Figure 12

Map views of V_s at different depths (indicated *above the panels*) obtained from Rayleigh waves dispersions. The velocity scale is in km/s and is variable for increased visual resolution. Clear velocity contrasts are observed across the SJFZ, the southern SAF, and the southern Elsinore fault. The SJFZ and the SAF are marked with low-velocity zones in the top 5 km; associated with damage zones and basins. The complex region associated with the merging SJFZ and SAF presents of strong velocity reduction in the top 5 km

zones associated with the SAF and Elsinore fault are observed, may also explain the differences between the results for Rayleigh and Love waves.

To improve the inversion results, we proceed by inverting V_s at each grid cell starting from the local high-resolution model of ALLAM and BEN-ZION (2012). For cells not covered by that model we use the average depth-dependent results as above. The data misfits over all cells and periods are small, usually bellow ± 0.05 km/s for Rayleigh waves (Fig. 11g). The inversions of Love waves group velocity maps have slightly higher misfits, usually within ± 0.1 km/s (Fig. 11h). As the misfit values are close to the errors of the dispersion measurements,

the results obtained are well defined for the range of periods used.

5.2. V_s Maps and Profiles

Figures 12 and 13 show, respectively, map views of the V_s values at different depths derived from the group velocities of the Rayleigh and Love waves. As in Figs. 8 and 9, we observe complex structures that include several features of interest. The SJFZ is well marked with low-velocity zones and velocity contrasts across the fault. In the section to the SE of the San Jacinto basin the NE block has higher V_s values, and the sense of velocity contrast is reversed across

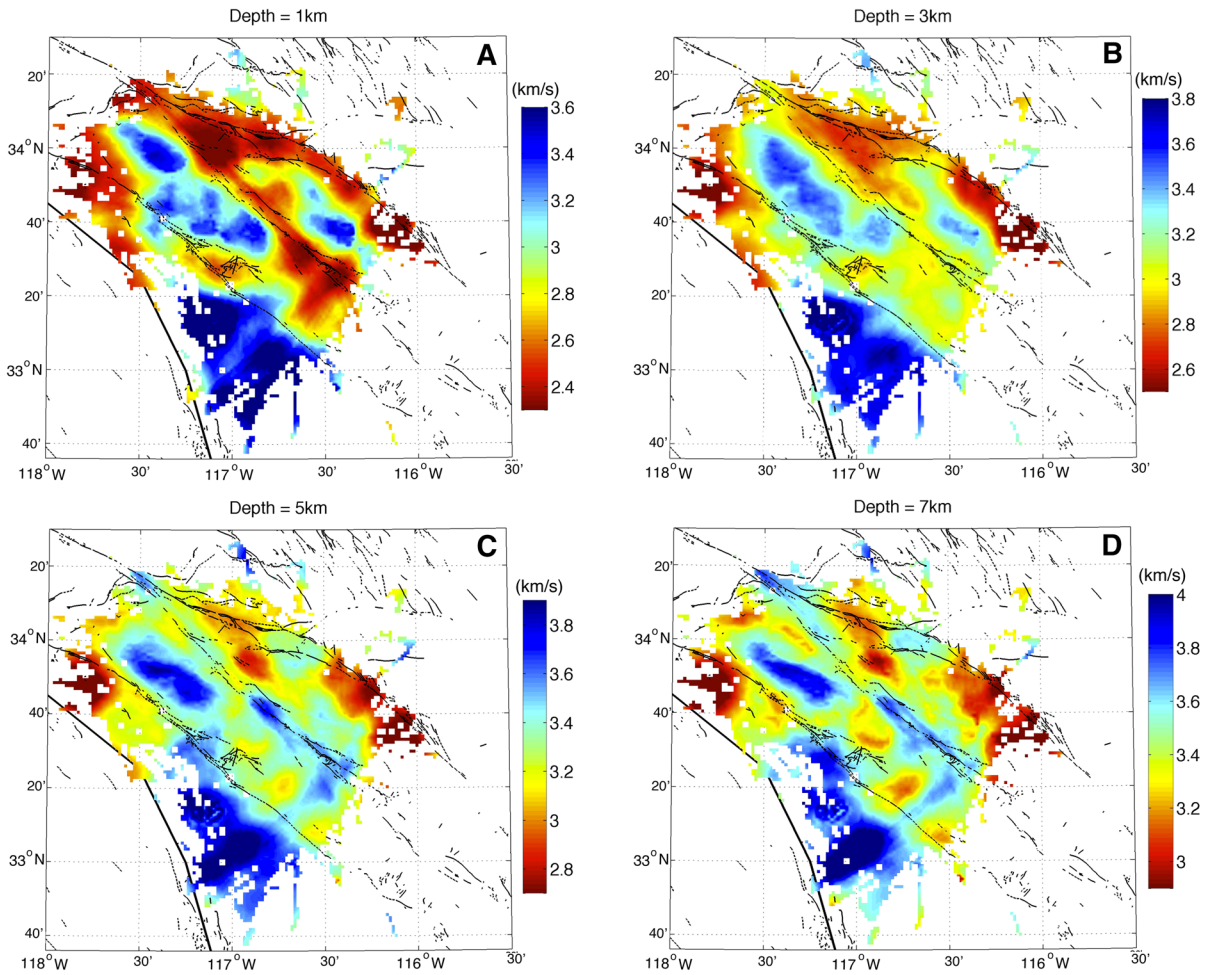


Figure 13

Map views of V_s at different depths obtained from Love waves dispersions. The velocity scale is in km/s and is variable for increased visual resolution. As shown in Fig. 11f the resolution at 7 km is poor. The results reveal clear velocity contrast and low-velocity zones associated with the main faults that are consistent with those obtained with Rayleigh waves (Fig. 12)

the section between the San Jacinto basin and the SAF. Velocity contrasts are also observed across the southern part of the SAF and the southern section of the Elsinore fault, with faster SW blocks in both cases. Both the SAF and SJFZ have prominent low-velocity zones in the top 5 km in areas of structural complexity, which extend to 7 km in the region between the two faults and the Salton trough area. Another interesting low-velocity zone extends near the SE edge of the model from the trifurcation area of the SJFZ toward the Elsinore fault. This feature is very pronounced at 1–3 km in the maps based on Love waves (Fig. 13). At a depth of 7 km, the most pronounced features in the results based on Rayleigh

waves are the low-velocity zones between the SAF and SJFZ, and SW of the SAF close to the Salton trough (Fig. 12d). In general, the tomographic images from the Rayleigh and Love waves have very consistent results on complex structures in the top 5 km of the plate-boundary region. Some of the discussed features are better shown in the fault-normal cross-sections presented in Figs. 14 and 15.

Figures 14 and 15 show V_s images based on Rayleigh and Love waves, respectively, for the fault-normal cross-sections marked as profiles 1–7 in Fig. 1. Profiles 1–4 go through the complex damage region between the SAF and SJFZ; and exhibit low velocities in the top 2–4 km, that are primarily on the

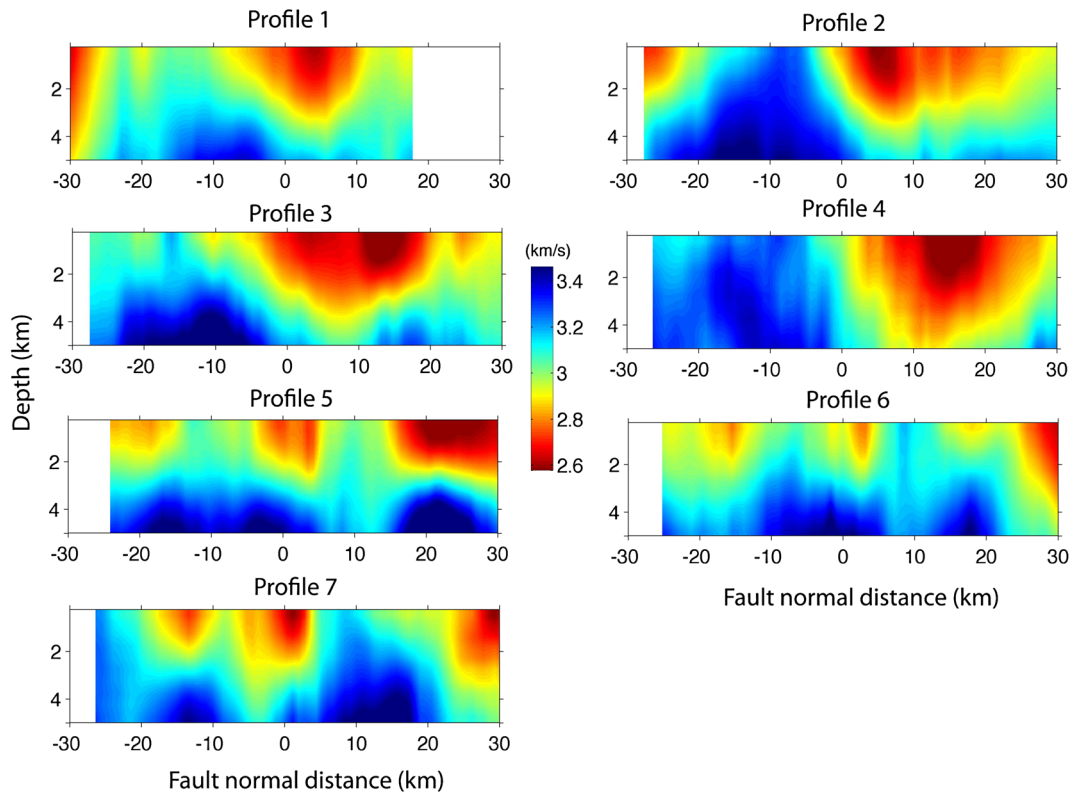


Figure 14

Fault-normal cross-sections of the shear wave velocity extracted from the Rayleigh wave model. The *zeros* indicate the position of the SJFZ on each profile. The locations of the cross-sections are plotted in Fig. 1. The velocity scale is in km/s and is the same for all panels. Lateral and depth variations of velocity contrasts and low velocity zones are observed. A broad velocity reduction that extend down to 4 km depth is associated with the complex region in which the SJFZ and SAF merge (profiles 3 and 4)

NE side of the SJFZ. Profiles 2–4 reveal a strong velocity contrast across the SJFZ that coincides with the surface trace of the fault. The velocities to the NE at these locations are reduced by up to 40 % in the top 4 km. As shown in Fig. 1, the region between the SAF and SJFZ has high seismicity that is broadly distributed with hypocentral depths between 4 and 20 km (HAUKSSON *et al.* 2012). We therefore observe spatial correlation between strong shear wave velocity reduction at shallow depths and diffuse seismicity at seismogenic depth. Profiles 5–6 show the effect of the San Jacinto Basin that reduces V_s strongly in the top 2 km on both sides of the main surface trace (Clark fault). Profile 7 crosses the trifurcation point and reveals a low-velocity zone (LVZ) in the top 2 km on both sides of the Clark fault. The entire trifurcation area is associated with high seismicity (Fig. 1), showing, again, a spatial correlation between shear wave velocity reduction in the top few km and

diffuse seismicity at depth. The widths of the LVZ decrease with depth, especially in the images associated with Love waves (Fig. 15), leading to flower shape structures.

The results obtained from the Love wave dispersion curves are in general agreement with the Rayleigh wave-based results. Most of the observed features with both wave types (low velocity fault damage zones, velocity contrasts and basin effects) are consistent. The overall lower resolution of the Love wave leads to more diffuse V_s images. As discussed for the average model, the shear wave velocities are usually lower by a few percent for the Love waves, because of larger velocity reductions near basins or fault zones at shallow depth (1–3 km). This may reflect the higher sensitivity of Love waves to shallow structures; they are more affected by the damage zones and basins in the top few km. The obtained shear wave velocity results are provided in the supplementary material.

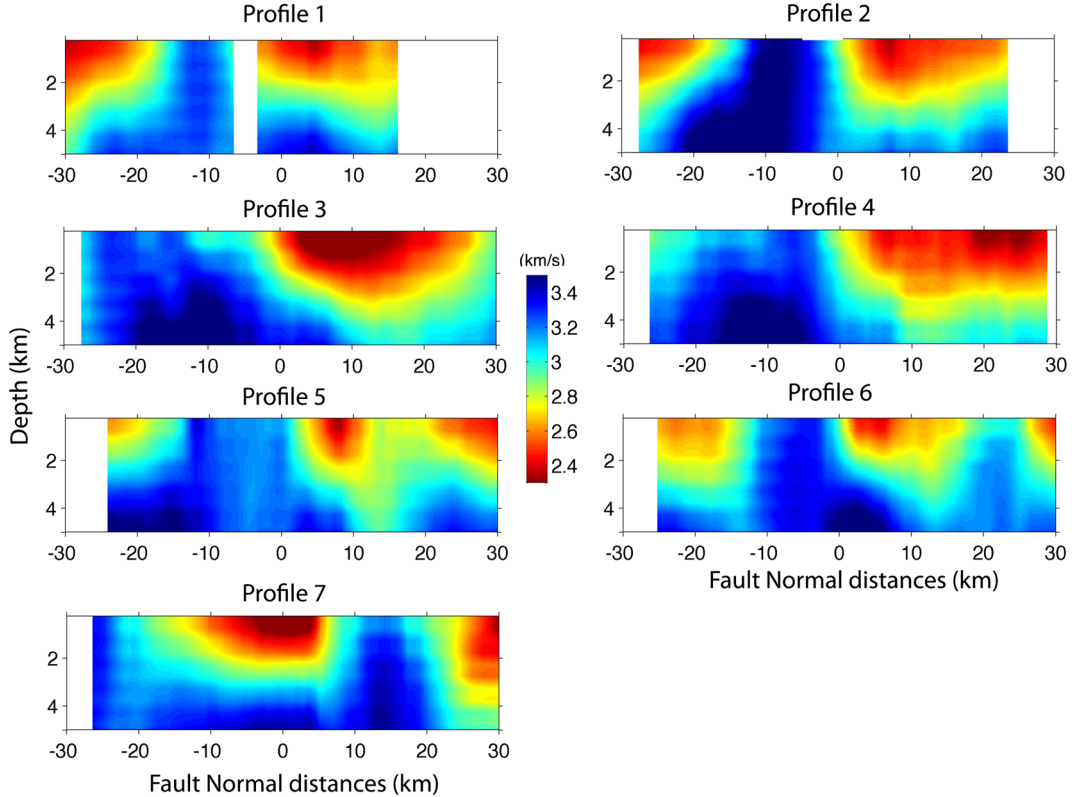


Figure 15

Fault-normal cross-sections of the shear wave velocity extracted from the Love wave model. The *zeros* indicate the position of the SJFZ on each profile. The velocity scale is in km/s and is the same for all panels. The observed velocity contrasts and damage zones are in good agreement with the results obtained from Rayleigh waves (Fig. 14)

6. Discussion and Conclusions

We performed detailed imaging of seismic velocity structures in the top ~ 7 km of the plate boundary region in southern California using noise-based Rayleigh and Love waves. The results complement earthquake tomography studies in the region (e.g. HAUSSON 2000; LIN *et al.* 2007; ALLAM and BEN-ZION 2012), which have low resolution in the top 2–3 km and in horizontal sections not covered well by propagation paths associated with earthquakes. The observed velocity structures primarily correlate with surface geology, with higher V_s in plutonic rocks (SHARP 1967), for example the Thomas Mountain Pluton on the NE block of the SJFZ near Anza. Our tomographic images reveal a variety of additional fault zone features (velocity contrasts, damage zones, basins, anisotropy) that are usually in good agreement with the detailed earthquake tomography studies of

the SJFZ environment (ALLAM and BEN-ZION 2012; ALLAM *et al.* 2014) and larger-scale imaging with earthquake and noise data (TAPE *et al.* 2010; RITZWOLLER *et al.* 2011; LIN *et al.* 2010).

The dispersion measurements of the Rayleigh and Love waves indicate (Figs. 5, 6) the existence of 2θ azimuthal anisotropy, which is approximately 6–10 % at 7 s period, with overall coast-perpendicular fast directions (approx. 200°). The results are generally consistent with large scale anisotropy studies in the region (e.g. LIN *et al.* 2011; ALVIZURI and TANIMOTO 2011), and reveal additional smaller scale features correlated with various elements of fault structures. The fast directions tend to align with the direction of the main strike-slip faults, but exhibit strong rotations near major complexities, for example the trifurcation area and the region between the SJFZ and SAF. Reduction of azimuthal anisotropy is observed for the geometrically simpler Anza section

of the SJFZ. Some aspects of the derived azimuthal anisotropy may be affected by the strong directionality of the noise sources in the area (e.g. SCHULTE-PELKUM *et al.* 2004; HILLERS *et al.* 2013). However, the correlations between spatial variations of the observed azimuthal anisotropy and various structural features suggest an overall physical origin of the discussed results, involving fault-parallel shearing and various perturbations near major fault complexities.

The obtained images for shear wave velocities reveal clear velocity contrasts across the SJFZ and Elsinore fault, with low-velocity zones around the SJFZ and SAF that are especially pronounced in the region between the two faults, around the San Jacinto basin, the trifurcation area of the SJFZ, and in the Salton trough area (Figs. 12, 13, 14, 15, 16). Shallow low-velocity zones also appear to extend from the SJFZ toward the Elsinore fault in the top 1–2 km. For the 3–7 km depth range, for which both our study and ALLAM and BEN-ZION (2012) tomography provide reliable images, there is good agreement in the locations of the velocity reductions associated with basins and damage zones, although their lateral extent is larger in our study because of the larger near-fault grid size used. As shown by the average model in Fig. 11a, our results are generally slower, by about 2–10 % at different depths, than those of ALLAM and BEN-ZION (2012). The differences between the two models decrease with increasing depth, suggesting the different depth resolution of the studies may explain the discrepancy. The earthquake tomography has good resolution from approximately 3 km to approximately 15 km (ALLAM and BEN-ZION 2012) while our noise-based surface waves imaging with periods between 3 and 12 s is mostly sensitive to the top ~ 7 km of the crust. The resolution of the earthquake tomography in the top 3 km is poor, because of the almost vertical ray paths, so the inversion results of ALLAM and BEN-ZION (2012) for the shallow crust are likely influenced by the deeper structures (overestimated). Similarly, our inversion results likely project shallower structures somewhat deeper, leading to underestimated velocities. Systematic study of the sensitivity of both inversion methods to depth is needed to understand better the generally slower V_s values obtained in our analysis.

Our noise-based tomography allows us to image velocity contrasts across a variety of fault sections (Figs. 14, 15) and flower-shape damage zones (Fig. 16) almost up to the surface. We observe higher V_s values on the NE block of the central section of the SJFZ, and a reversed contrast on the section between the San Jacinto basin and the SAF. Similar contrasts have been observed over seismogenic depth sections by ALLAM and BEN-ZION (2012) and ALLAM *et al.* (2014). As discussed in those papers, the observed velocity contrasts combined with model results for bimaterial ruptures (e.g. BEN-ZION and ANDREWS 1998; SHI and BEN-ZION 2006; AMPUERO and BEN-ZION 2008) imply a statistically preferred rupture direction of earthquakes on the central section of the SJFZ to the NW. This inference is consistent with observed rock damage asymmetry across the fault (DOR *et al.* 2006; LEWIS *et al.* 2005; WECHSLER *et al.* 2009), along-strike asymmetry of aftershocks (ZALIAPIN and BEN-ZION 2011), and reversed-polarity secondary deformation structures near segment ends (BEN-ZION *et al.* 2012). The reversed velocity contrast NW of the San Jacinto basin, with higher velocity in the SW block, may act as a dynamic barrier by increasing the normal stress at the tip of NW-propagating ruptures that nucleate around Anza or in the trifurcation area. We also observe a clear velocity contrast across the SE part of the Elsinore fault with higher V_s on the SW side, and little or possibly reversed contrast on the NW section of the fault. The validity of these results for the deeper sections of the Elsinore fault should be substantiated with detailed earthquake tomography or noise imaging using longer periods.

The flower-shape damage zones around the SJFZ and SAF in Fig. 16, with broader damage around geometrical fault zone complexities, merge nicely with the images of ALLAM and BEN-ZION (2012) and are consistent with theoretical results on decreasing damage width with depth (e.g. BEN-ZION and SHI 2005; FINZI *et al.* 2009; KANEKO and FIALKO 2011). It is interesting to note that the broad damage zone in the region between the SJFZ and SAF, with up to 40 % velocity reduction in the top few km, corresponds to a zone of high diffuse seismicity at seismogenic depth (HAUKSSON *et al.* 2012). A similar correlation between a significant broad shallow damage zone and deep diffuse seismicity is also

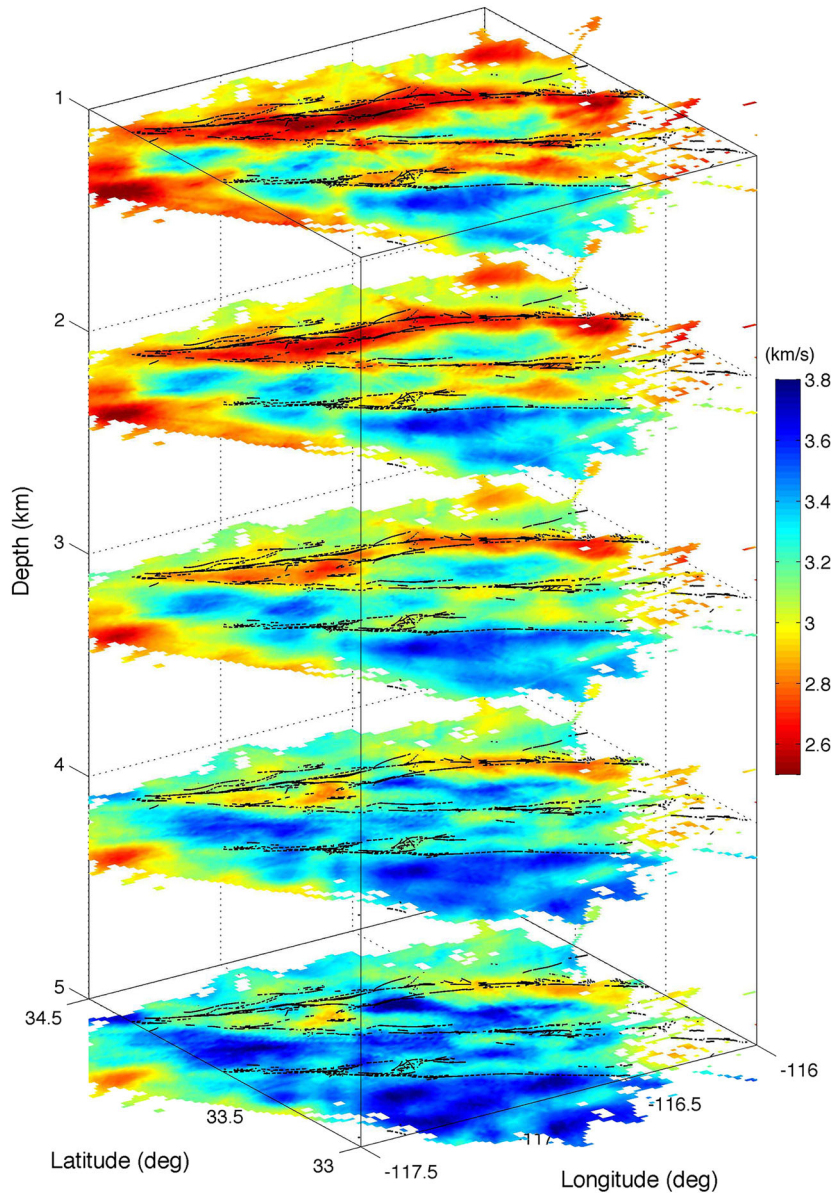


Figure 16

A composite 3D image of shear wave velocities (*colors*) in the SJFZ, obtained from inversion of Rayleigh waves group velocities. Clear velocity contrasts and low velocity zones following flower-shape with depth are observed

observed in the complex trifurcation area that is associated with highly heterogeneous focal mechanisms (BAILEY *et al.* 2010; HAUSSON *et al.* 2012). The broad damage zones are generally relic structures reflecting the early organizational stage of the fault zone (e.g. BEN-ZION and SAMMIS 2003). The correlation of such zones with the diffuse seismicity can be explained by remaining geometrical heterogeneities

that persist at seismogenic depth and produce local stress concentrations that initiate ruptures.

The noise-based tomographic results reported in this paper significantly improve available information on seismic velocities in the top ~ 7 km of the complex plate boundary region around the SJFZ. More detailed imaging of the velocity structure in the top 500 m may be obtained using correlations of coda

waves (e.g. CAMPILLO and PAUL 2003), full earthquake waveforms (ROUX and BEN-ZION 2014), or high-frequency noise. Integrating the imaging results associated with the available earthquake and noise data is best done by performing joint inversions of the different measurements. This will be attempted in follow up work.

Acknowledgments

The data used in this work were recorded mostly by the Southern California Seismic Network operated by Caltech and USGS. We also used data recorded near the SJFZ by a temporary NSF-CD deployment operated by the University of California, San Diego, and data recorded by the University of California, Santa Barbara. We thank Amir Allam, Gregor Hillers, Nikolai Shapiro, Laurent Stehly, and Frank Vernon for useful discussions. We also thank Martha Savage, an anonymous referee, and Editor Antonio Rovelli for constructive comments. The study was supported by the National Science Foundation (grant EAR-0908903). MC and PR acknowledge support from the European Research Council (advanced grant 227507 “Whisper”).

REFERENCES

- ALLAM, A. A. and Y. BEN-ZION (2012), *Seismic velocity structures in the Southern California plate-boundary environment from double-difference tomography*, *Geophys. J. Int.*, *190*, 1181–1196, doi:[10.1111/j.1365-246X.2012.05544.x](https://doi.org/10.1111/j.1365-246X.2012.05544.x).
- ALLAM, A. A., Y. BEN-ZION I. KURZON and F. L. VERNON (2014), *Seismic velocity structure in the Hot Springs and Trifurcation Seismicity Cluster Areas of the San Jacinto Fault Zone from double-difference tomography*, *Geophys. J. Int.*, *198*, 978–999, doi:[10.1093/gji/ggu176](https://doi.org/10.1093/gji/ggu176).
- ALVIZURI, C. and T. TANIMOTO, (2011). *Azimuthal anisotropy from array analysis of Rayleigh waves in Southern California*. *Geophys. J. Int.*, *186*, B08307.
- AMPUERO, J.-P. and Y. BEN-ZION (2008). *Cracks, pulses and macroscopic asymmetry of dynamic rupture on a bimaterial interface with velocity-weakening friction*, *Geophys. J. Int.*, *173*, 674–692, doi:[10.1111/j.1365-246X.2008.03736.x](https://doi.org/10.1111/j.1365-246X.2008.03736.x).
- ASTER, R.C., SHEARER, P.M. and BERGER, J., (1990). *Quantitative measurements of shear wave polarizations at the Anza seismic network, southern California: Implications for shear wave splitting and earthquake prediction*, *J. Geophys. Res.*, *95*, 12 449–12 473.
- BAILEY, I. W., BEN-ZION, Y., BECKER, T. W. and HOLSCHNEIDER, M. (2010), *Quantifying focal mechanism heterogeneity for fault zones in central and southern California*. *Geophysical Journal International*, *183*: 433–450. doi:[10.1111/j.1365-246X.2010.04745.x](https://doi.org/10.1111/j.1365-246X.2010.04745.x).
- BARMIN, M., M. RITZWOLLER, and A. LEVSHIN (2001), *A fast and reliable method for surface wave tomography*, *Pure Appl. Geophys.*, *158*(8), 1351–1375.
- BENSEN G.D., RITZWOLLER M.H., BARMIN M.P., LEVSHIN A. L., LIN F., MOSCHETTI M. P, SHAPIRO N. M. YANG Y., (2007), *Processing seismic ambient noise data to obtain reliable broad-band surface wave dispersion measurement*, *Geophys. J. Int.*, *169*, 1239–1260.
- BEN-ZION, Y. (2008). *Collective behavior of earthquakes and faults: continuum-discrete transitions, evolutionary changes and corresponding dynamic regimes*, *Rev. Geophys.*, *46*, RG4006, doi:[10.1029/2008RG000260](https://doi.org/10.1029/2008RG000260).
- BEN-ZION, Y. and D. J. ANDREWS, (1998), *Properties and Implications of Dynamic Rupture Along a Material Interface*, *Bull. Seism. Soc. Am.*, *88*, 1085–1094.
- BEN-ZION, Y., T. ROCKWELL, Z. SHI and S. XU, (2012). *Reversed-polarity secondary deformation structures near fault stepovers*, *J. of Appl. Mech.*, *79*, 031025, doi:[10.1115/1.4006154](https://doi.org/10.1115/1.4006154).
- BEN-ZION, Y. and C.G. SAMMIS (2003). *Characterization of fault zones*, *Pure appl. Geophys.*, *160*, 677–715.
- BEN-ZION, Y. and Z. SHI (2005). *Dynamic rupture on a material interface with spontaneous generation of plastic strain in the bulk*, *Earth Planet. Sci. Lett.*, *236*, 486–496, doi:[10.1016/j.epsl.2005.03.025](https://doi.org/10.1016/j.epsl.2005.03.025).
- BOORE, D.M. (2014). *What do data used to develop ground-motion prediction equations tell us about motions near faults?*, *Pure and Applied Geophysics*, doi:[10.1007/s00024-013-0748-9](https://doi.org/10.1007/s00024-013-0748-9).
- BONESS N.L. and M.D. ZOBACK, (2006). *A multiscale study of the mechanisms controlling shear velocity anisotropy in the San Andreas Fault Observatory at Depth*. *Geophysics*, *71*, doi:[10.1190/1.2231107](https://doi.org/10.1190/1.2231107).
- BOUÉ P., P. ROUX, M. CAMPILLO and B. de CACQUERAY (2013) *Double beamforming processing in a seismic prospecting context*. *Geophysics*. Volume: 78 Issue: 3 Pages: V101–V108 doi:[10.1190/GEO2012-0364.1](https://doi.org/10.1190/GEO2012-0364.1).
- CAMPILLO, M. and A PAUL, (2003), *Long-range correlations in the seismic coda*, *Science* *299*, 547–549.
- CAMPILLO, M., ROUX, P. and SHAPIRO, N.M., (2011), Using seismic noise to image and to monitor the Solid Earth, in *Encyclopedia of Solid Earth Geophysics*, ed. Gupta, Harsh K., pp. 1230–1235, Springer.
- CAMPILLO, M., S. SINGH, N. SHAPIRO, J. PACHECO, and R. HERRMANN (1996). *Crustal structure south of the Mexican volcanic belt, based on group velocity dispersion*, *Geofis. Int.*, *35*, 361–370.
- DAIR, L., and COOKE, M.L., (2009), *San Andreas fault geometry through the San Geronio Pass, California: The Geological Society of America*, v. 37; no. 2, p.119–122.
- DOR, O., ROCKWELL, T.K. and BEN-ZION, Y., (2006). *Geologic observations of damage asymmetry in the structure of the San Jacinto, San Andreas and Punchbowl faults in southern California: a possible indicator for preferred rupture propagation direction*, *Pure appl. Geophys.*, *163*, 301–349, doi:[10.1007/s00024-005-0023-9](https://doi.org/10.1007/s00024-005-0023-9).
- FAY, N.P. and HUMPHREYS, E.D., (2005). *Fault slip rates, effects of elastic heterogeneity on geodetic data, and the strength of the lower crust in the Salton Trough region, southern California*, *J. geophys. Res.*, *110*, B09401, doi:[10.1029/2004JB003548](https://doi.org/10.1029/2004JB003548).
- FIALKO, Y., L. RIVERA, and H. KANAMORI, (2005). *Estimate of differential stress in the upper crust from variations in topography and strike along the San Andreas fault*, *Geophys. J. Int.*, *160*, 527–532.

- FINZI, Y., HEARN, E.H., LYAKHOVSKY, V. and Y. BEN-ZION (2009). *Structural properties and deformation patterns of evolving strike-slip faults: numerical simulations incorporating damage rheology*, Pure appl. Geophys., 166, 1537–1573, doi:[10.1007/s00024-009-0522-1](https://doi.org/10.1007/s00024-009-0522-1).
- FROMENT B., CAMPILLO M., ROUX P., GOUEDARD P., VERDEL A., WEAVER R.L. (2010), *Estimation of the effect of nonisotropically distributed energy on the apparent arrival time in correlations*, Geophysics, 75, SA85–SA93, doi:[10.1190/1.3483102](https://doi.org/10.1190/1.3483102).
- FRY, B., F. DESCHAMPS, E. KISSLING, L. STEHLY, and D. GIARDINI (2010), *Layered azimuthal anisotropy of Rayleigh wave phase velocities in the European Alpine lithosphere inferred from ambient noise*, Earth Planet. Sci. Lett., 297(1), 95–102.
- FUIS, S. G., D. SCHEIRERS, E. V. LANGENHEIM, D. M. KOHLER, (2012). *A New Perspective on the Geometry of the San Andreas Fault of South California and Relationship to Lithospheric Structure*, Bulletin of Seismological Society of America, Vol. 102, 2012, pp. 236–251.
- HANSEN, P. and O'LEARY, D., (1993). *The use of the L-Curve in the regularization of discrete ill-posed problems*, SIAM J. Sci. Comput., 14, 1487–1503.
- HAUKSSON, E. (2000), *Crustal structure and seismicity distribution adjacent to the Pacific and North America plate boundary in southern California*, J. Geophys. Res., 105, 13,875–13,903.
- HAUKSSON, E., W. YANG, and P. M. SHEARER, (2012). *Waveform Relocated Earthquake Catalog for Southern California (1981 to June 2011)*; Bull. Seismol. Soc. Am., Vol. 102, No. 5, doi:[10.1785/0120120010](https://doi.org/10.1785/0120120010).
- HERMAN, R.B. and AMMON, C.J., (2002). *Surface Waves, Receiver Function and Crustal Structure*, St. Louis University.
- HILLERS, G. and Y. BEN-ZION, (2011), *Seasonal variations of observed noise amplitudes at 2-18 Hz in southern California*, Geophys. J. Int., 184, 860–868, doi: [10.1111/j.1365-246X.2010.04886.x](https://doi.org/10.1111/j.1365-246X.2010.04886.x).
- HILLERS, G., Y. BEN-ZION, M. LANDÈS, and M. CAMPILLO (2013), *Interaction of microseisms with crustal heterogeneity: A case study from the San Jacinto fault zone area*, Geophys. Geosyst., 14, 2182–2197, doi:[10.1002/ggge.20140](https://doi.org/10.1002/ggge.20140).
- JANECKE, S.U., DORSEY, R.J., and BELGARDE, B., (2010). *Age and structure of the San Jacinto and San Felipe fault zones and their lifetime slip rates*: In Clifton, H.E., and Ingersoll, R.V., eds., 2010, *Geologic excursions in California and Nevada: tectonics, stratigraphy and hydrogeology*: Pacific Section, SEPM (Society for Sedimentary Geology) Book 108, p. 233–271.
- KANEKO, Y., and FIALKO Y., (2011). *Shallow slip deficit due to large strike-slip earthquakes in dynamic rupture simulations with elasto-plastic off-fault response*. Geophysical Journal International. 186:1389–1403.
- KIMMAN W.P. and TRAMPERT J., (2010). *Approximations in seismic interferometry and their effects on surface waves*, Geophys. J. Int., 182, 461–476.
- KIRBY, S.M., JANECKE, S.U., DORSEY, R.J., HOUSEN, B.A., MCDUGALL, K., LANGENHEIM, V., and STEELY, A. (2007). *Pleistocene Brawley and Ocotillo formations: evidence for initial strike-slip deformation along the San Felipe and San Jacinto fault zones*, Calif. J. Geol. 115, 43–62.
- KURZON, I., F.L. VERNON, Y. BEN-ZION and G. ATKINSON, (2014). *Ground Motion Prediction Equations in the San Jacinto Fault Zone—Significant Effects of Rupture Directivity and Fault Zone Amplification*, Pure Appl. Geophys., doi:[10.1007/s00024-014-0855-2](https://doi.org/10.1007/s00024-014-0855-2).
- LANDÈS, M., HUBANS, F., SHAPIRO, N., PAUL, A. AND CAMPILLO, M., (2010). *Origin of deep ocean microseisms by using teleseismic body waves*, J. geophys. Res., 115, B05302, doi:[10.1029/2009JB006918](https://doi.org/10.1029/2009JB006918).
- LEVSHIN, A., YANOVSKAYA, T., LANDER, A., BURCHIN, B., BARMIN, M., RATNIKOVA, L. AND ITS, E., (1989). *Seismic Surface Waves in a Laterally Inhomogeneous Earth*, Kluwer, Dordrecht.
- LEWIS, M.A., PENG, Z., BEN-ZION, Y. and VERNON, F.L., (2005). *Shallow seismic trapping structure in the San Jacinto fault zone near Anza, California*, Geophys. J. Int., 162, 867–881, doi:[10.1111/j.1365-246X.2005.02684.x](https://doi.org/10.1111/j.1365-246X.2005.02684.x).
- LIN, F., MOSCHETTI, M. AND RITZWOLLER, M., (2008). *Surface wave tomography of the western United States from ambient seismic noise: Rayleigh and Love wave phase velocity maps*, Geophys. J. Int., 173(1), 281–298.
- LIN, F., RITZWOLLER, M., TOWNEND, J., BANNISTER, S. and SAVAGE, M., (2007). *Ambient noise Rayleigh wave tomography of New Zealand*, Geophys. J. Int., 170(2), 649–666.
- LIN, F., RITZWOLLER, M. H. and SNIEDER, R. (2009), *Eikonal tomography: surface wave tomography by phase front tracking across a regional broad-band seismic array*. Geophysical Journal International, 177:1091–1110. doi:[10.1111/j.1365-246X.2009.04105.x](https://doi.org/10.1111/j.1365-246X.2009.04105.x).
- LIN, F., M. RITZWOLLER, Y. YANG, M. MOSCHETTI, and M. FOUCH (2011), *Complex and variable crustal and uppermost mantle seismic anisotropy in the western United States*, Nat. Geosci., 4(1), 55–61.
- LIN, G., THURBER, C.H., ZHANG, H., HAUSSON, E., SHEARER, P., WALDHAUSER, F., BROCHER, T.M. and HARDEBECK, J., (2010). *A California statewide three dimensional seismic velocity model from both absolute and differential times*, Bull. seism. Soc. Am., 100, 225–240.
- LIN, G., P. M. SHEARER, E. HAUSSON, and C. H. THURBER (2007), *A three-dimensional crustal seismic velocity model for southern California from a composite event method*, J. Geophys. Res., 112, B11306, doi:[10.1029/2007JB004977](https://doi.org/10.1029/2007JB004977).
- LINDSEY, E. O., and Y. FIALKO (2013), *Geodetic slip rates in the southern San Andreas Fault system: Effects of elastic heterogeneity and fault geometry*, J. Geophys. Res. Solid Earth, 118, 689–697, doi:[10.1029/2012JB009358](https://doi.org/10.1029/2012JB009358).
- LIU, Y., T. L. TENG and Y. BEN-ZION, (2005). *Near-surface seismic anisotropy, attenuation and dispersion in the aftershock region of the 1999 Chi-Chi, earthquake*, Geophys. J. Int., 160, 695–706.
- MAGISTRALE, H., and C. SANDERS (1996), *Evidence from precise earthquake hypocenters for segmentation of the San Andreas Fault in San Geronio Pass*, J. Geophys. Res., 101(B2), 3031–3044, doi:[10.1029/95JB03447](https://doi.org/10.1029/95JB03447).
- MARILYANI, G.I., ROCKWELL, T.K., ONDERDONK, N.H., AND MCGILL, S.F (2013). *Straightening of the Northern San Jacinto Fault, California as Seen in the Fault-structure Evolution of the San Jacinto Valley Stepover*, Bull. Seismol. Soc. Am. 103(3).
- MORDRET, A., N. M. SHAPIRO, S. SINGH, P. ROUX, J.P. MONTAGNER and O. I. BARKVED, (2013). *Azimuthal anisotropy at Valhall: the Helmholtz equation approach*, Geophysical Research Letter, doi:[10.1002/grl.50447](https://doi.org/10.1002/grl.50447).
- MORTON, N., GIRTY, G.H. and ROCKWELL, T.K., (2012). *Fault zone architecture of the San Jacinto fault zone in Horse Canyon, southern California: a model for focused post-seismic fluid flow and heat transfer in the shallow crust*, Earth planet. Sci. Lett., 330, 71–83, doi:[10.1016/j.espl.2012.02.0](https://doi.org/10.1016/j.espl.2012.02.0).
- MORTON, D.M., and MATTI, J.C., (1993), *Extension and contraction within an evolving divergent strike-slip fault complex: The San Andreas and San Jacinto fault zones at their convergence in*

- southern California, in Powell, R.E., Weldon, R.J.,II, and Matti, J.C., eds., *The San Andreas fault system: Displacement, palinspastic reconstruction, and geologic evolution*: Geological Society of America, Memoir 178, Chapter 5, p. 217–230.
- MOSCHETTI, M., RITZWOLLER, M. AND SHAPIRO, N., (2007). *Surface wave tomography of the western United States from ambient seismic noise: Rayleigh wave group velocity maps*, *Geochem. Geophys. Geosyst.*, 8, Q08010, doi:[10.1029/2007GC001655](https://doi.org/10.1029/2007GC001655).
- ONDERDONK, N.W. (1998). *The tectonic structure of the Hot Springs fault zone, Riverside County, California* [Ph.D. Thesis]: California State University, Long Beach, California.
- PENG, Z., and Y. BEN-ZION (2004), *Systematic analysis of crustal anisotropy along the Karadere-Düzce branch of the north Anatolian fault*, *Geophys. J. Int.*, 159, 253–274, doi:[10.1111/j.1365-246X.2004.02379.x](https://doi.org/10.1111/j.1365-246X.2004.02379.x).
- POLI P., H. A. PEDERSEN, M. CAMPILLO, and the POLENET/LAPNET Working Group (2012), *Noise directivity and group velocity tomography in a region with small velocity contrasts : the northern Baltic Shield*. *Geophysical Journal International* 192, 413–424.
- RITZWOLLER, M.H., F.C. LIN, and W. SHEN (2011), *Ambient noise tomography with a large continental seismic array*, *Compte Rendus Geoscience*, 13 pages, doi:[10.1016/j.crte.2011.03.007](https://doi.org/10.1016/j.crte.2011.03.007).
- ROCKWELL, T., LOUGHMAN, C. and MERIFIELD, P., (1990). *Late Quaternary rate of slip along the San Jacinto fault zone near Anza, Southern California*, *J. geophys. Res.* B, 95(6), 8593–8605.
- ROCKWELL, T.K., SEITZ, G.G., DAWSON, T.E. and YOUNG, J., (2006). *The long record of San Jacinto Fault paleoearthquakes at Hog Lake; implications for regional patterns of strain release in the southern San Andreas Fault system*, *Seismol. Res. Lett.*, 77, 270–296.
- ROCKWELL, T. K., T. E. DAWSON, J. YOUNG and GORDON SEITZ (2014), *A 21 event, 4,000-year history of surface ruptures in the Anza Seismic Gap, San Jacinto Fault: Implications for long-term earthquake production on a major plate boundary fault*, *Pure Appl. Geophys.*, in review.
- ROUX, P. and Y. BEN-ZION, (2014). *Monitoring fault zone environments with correlations of earthquake waveforms*, *Geophys. J. Int.*, 196, 1073–1081, doi:[10.1093/gji/ggt441](https://doi.org/10.1093/gji/ggt441).
- ROUX, P., WATHELET, M. and ROUEFF, A., (2011). *The San Andreas Fault revisited through seismic-noise and surface-wave tomography*, *Geophys. Res. Lett.*, 38, L13319, doi:[10.1029/2011GL047811](https://doi.org/10.1029/2011GL047811).
- SABRA, K. G., P. GERSTOFT, P. ROUX, W. A. KUPERMAN, and M. C. FEHLER (2005a), *Extracting time-domain Greens function estimates from ambient seismic noise*, *Geophys. Res. Lett.*, 32, L03310, doi:[10.1029/2004GL021862](https://doi.org/10.1029/2004GL021862).
- SABRA, K. G., P. GERSTOFT, P. ROUX, W. A. KUPERMAN, and M. C. FEHLER (2005b), *Surface wave tomography from microseisms in Southern California*, *Geophys. Res. Lett.*, 32, L14311, doi:[10.1029/2005GL023155](https://doi.org/10.1029/2005GL023155).
- SALISBURY, J.B., ROCKWELL, T.K., MIDDLETON, T.J. and HUDNUT, K.W., (2012). *LiDAR and field observations of slip distribution for the most recent surface ruptures along the central San Jacinto Fault*, *Bull. seism. Soc. Am.*, 102, 598–619, doi:[10.1785/0120110068](https://doi.org/10.1785/0120110068).
- SCHULTE-PELKUM, V., P. S. EARLE, and F. L. VERNON (2004), *Strong directivity of ocean-generated seismic noise*, *Geochem. Geophys. Geosyst.*, 5, Q03004, doi:[10.1029/2003GC000520](https://doi.org/10.1029/2003GC000520).
- SEEBER, L., and J. G. ARMBRUSTER (1995), *The San Andreas Fault system through the Transverse Ranges as illuminated by earthquakes*, *J. Geophys. Res.*, 100(B5), 8285–8310, doi:[10.1029/94JB02939](https://doi.org/10.1029/94JB02939).
- SHAPIRO, N. and CAMPILLO, M., (2004). *Emergence of broadband Rayleigh waves from correlations of the ambient seismic noise*, *Geophys. Res. Lett.*, 31(7), doi:[10.1029/2004GL019491](https://doi.org/10.1029/2004GL019491).
- SHAPIRO, N.M., CAMPILLO, M., STEHLY, L. and RITZWOLLER, M.H., (2005). *High resolution surface-wave tomography from ambient seismic noise*, *Science*, 29, 1615–1617.
- SHARP, R.V., (1967). *San Jacinto fault zone in the Peninsular Ranges of south- ern California*, *Geol. Soc. Am. Bull.*, 78, 705–730.
- SHI, Z. and Y. BEN-ZION, (2006). *Dynamic rupture on a bimaterial interface governed by slip-weakening friction*, *Geophys. J. Int.*, 165, 469–484, doi:[10.1111/j.1365-246X.2006.02853.x](https://doi.org/10.1111/j.1365-246X.2006.02853.x).
- SMITH, M., and F. DAHLEN (1973), *The azimuthal dependence of Love and Rayleigh wave propagation in a slightly anisotropic medium*, *J. Geophys. Res.*, 78(17), 3321–3333.
- STEHLY, L, M. CAMPILLO and N. SHAPIRO (2006), *A Study of the seismic noise from its long-range correlation properties*, *Journal of Geophysical research*, Vol 111, B10306.
- STEHLY, L., FRY, B., CAMPILLO, M., SHAPIRO, N. M., GUILBERT, J., BOSCHI, L. and GIARDINI, D. (2009), *Tomography of the Alpine region from observations of seismic ambient noise*. *Geophysical Journal International*, 178: 338–350. doi:[10.1111/j.1365-246X.2009.04132.x](https://doi.org/10.1111/j.1365-246X.2009.04132.x).
- TAPE, C., Q. LIU, A. MAGGI, and TROMP, J., (2010). *Seismic tomography of the southern California crust based on spectral-element and adjoint methods*. *Geophys. J. Int.*, 180, 433–462.
- WECHSLER, N., ROCKWELL, T.K. and Y. BEN-ZION (2009). *Application of high resolution DEM data to detect rock damage from geomorphic signals along the central San Jacinto Fault*, *Geomorphology*, 113, 82–96, doi:[10.1016/j.geomorph.2009.06.007](https://doi.org/10.1016/j.geomorph.2009.06.007).
- WEAVER, R.L., B. FROMENT and M. CAMPILLO, (2009), *On the correlation of non-isotropically distributed ballistic scalar diffuse waves*: *Journal of the Acoustical Society of America*, 126 (4), 1817–1826, doi:[10.1121/1.3203359](https://doi.org/10.1121/1.3203359).
- YANG, H. and ZHU, L., (2010). *Shallow low-velocity zone of the San Jacinto fault from local earthquake waveform modelling*, *Geophys. J. Int.*, 183, 421–432.
- YANG, Y., RITZWOLLER, M., LEVSHIN, A. and SHAPIRO, N., (2007). *Ambient noise Rayleigh wave tomography across Europe*, *Geophys. J. Int.*, 168, 259–274.
- YANG, Z., A. SHEEHAN, and P. SHEARER (2011), *Stress induced upper crustal anisotropy in southern California*, *J. Geophys. Res.*, 116, B02302, doi:[10.1029/2010JB007655](https://doi.org/10.1029/2010JB007655).
- YULE, D., and K. SIEH (2003), *Complexities of the San Andreas fault near San Geronio Pass: Implications for large earthquakes*, *J. Geophys. Res.*, 108, 2548, doi:[10.1029/2001JB000451](https://doi.org/10.1029/2001JB000451), B11.
- ZALIAPIN, I. and Y. BEN-ZION, (2011). *Asymmetric distribution of aftershocks on large faults in California*, *Geophys. J. Int.*, 185, 1288–1304, doi: [10.1111/j.1365-246X.2011.04995.x](https://doi.org/10.1111/j.1365-246X.2011.04995.x).
- ZOBACK, M. and HEALY, J. (1992). *In Situ Stress Measurements to 3.5 km Depth in the Cajon Pass Scientific Research Borehole: Implications for the Mechanics of Crustal Faulting*. *Journal of Geophysical Research* 97: doi:[10.1029/91JB02175](https://doi.org/10.1029/91JB02175). issn: 0148-0227.